

**Electrospun materials for solar energy conversion:  
innovations and trends**

Journal:	<i>Journal of Materials Chemistry C</i>
Manuscript ID	TC-REV-02-2016-000702.R1
Article Type:	Review Article
Date Submitted by the Author:	23-Apr-2016
Complete List of Authors:	JOLY, Damien; CEA, INAC-SPRAM; CNRS, INAC-SPRAM; Univ. Grenoble Alpes, INAC-SPRAM Jung, Ji-Won; Korea Advanced Institute of Science and Technology, Department of Materials Science and Engineering Kim, Il-Doo; Korea Advanced Institute of Science and Technology, Materials Science and Engineering DEMADRILLE, Renaud; CEA, INAC-SPRAM; CNRS, INAC-SPRAM; Univ. Grenoble Alpes, INAC-SPRAM



## Electrospun materials for solar energy conversion: innovations and trends

Damien Joly,<sup>a,b,c</sup> Ji-Won Jung,<sup>d</sup> Il-Doo Kim<sup>d\*</sup> and Renaud Demadrille<sup>a,b,c\*</sup>

Received 00th February 2016,  
Accepted 00th January 20xx

DOI: 10.1039/x0xx00000x

[www.rsc.org/](http://www.rsc.org/)

This feature article discusses highly promising and versatile electrospinning methods and electrospun materials employed for the fabrication of solar cells. Electrospinning is attracting for creating one dimensional mesostructured organic, inorganic and hybrid nanomaterials of controlled dimensions, prepared as random or oriented continuous nanofibers (NFs), with possibilities of ordered internal morphologies such as core-sheath, hollow or porous fibre, or even multichanneled microtube arrangements. The dimensionality, directionality and compositional flexibility of electrospun NFs and mats are increasingly being investigated for the targeted development of electrode and electrolyte materials, where the specific properties associated with nanoscale features such as high surface area and aspect ratios, low density and high pore volume, allow performance improvements in solar energy conversion devices.

### 1. Introduction

During the last decade, the dramatic growth of advanced electronic and optoelectronic devices, and related technologies, has been inherently associated to the development of innovative nanomaterials. Around the world academic and industrial researchers have focused their works to design and synthesize new nanomaterials exhibiting tailor-made properties for various application domains including information and communication technologies,<sup>1,2</sup> biotechnologies and health care technologies,<sup>3</sup> sensors,<sup>4,5,6</sup> energy conversion and storage.<sup>7,8,9</sup>

In this particular field, nanostructured materials appear as valuable components to decrease the weight of energy storage devices such as batteries and supercapacitors,<sup>10,11,12</sup> or to boost the performances of photovoltaic and thermoelectric devices.<sup>13,14,15,16</sup> The preparation of nanomaterials requires from the scientists to develop specific methods and processes in order to control the shape of these nano-objects, their dimension and their chemical composition. Among the techniques and tools developed for the preparation of nanomaterials, electrospinning appears as one of the most powerful and versatile methods. Indeed this wonderful technique that was discovered more than one hundred years ago by Coley,<sup>17</sup> and later developed by Formhals,<sup>18</sup> allows for the fabrication of a large variety of nanostructured and mesostructured inorganic, organic, and hybrid materials.

Nowadays the tremendous interest of the scientific community in electrospinning originates first from its unique

capabilities in creating nanostructures from ceramic materials. This remarkably simple technique is applicable to all condensable materials, spanning from polymer solutions to molten materials and it allows the production of ceramic nanofibers (NFs) with either a dense, porous, or hollow structure when it is combined with conventional sol-gel processing followed by high temperature calcination. One of the strong advantages of the technique is the possibility to tune accurately the chemical composition and the dimensions of the synthesized nanomaterials. Besides, the control of the directional arrangement of the nano-objects as well as the surface coverage can be achieved on various surfaces.<sup>19</sup> From an applicative point of view electrospinning is a cost-effective method that can be easily scaled-up making it very economically attractive and compatible with industrial requirements.<sup>12</sup> For the above mentioned reasons, electrospinning methods were developed and employed in recent years for the fabrication of various material electrodes suitable for energy conversion and storage applications.<sup>20</sup>

In this review, we will discuss some of the most interesting features associated with electrospinning technique for the preparation of nanomaterials of interest, particularly for photovoltaic energy conversion. We will introduce the key principles of the electrospinning process and highlight the potentialities of electrospun materials by presenting the various morphologies that can be obtained, and the diverse compositions of binary or ternary metal oxide semiconductors or doped materials that can be achieved.

We will attempt to provide a detailed overview of the various materials made so far by electrospinning and shed light on the recent developments involving electrospun materials in emerging photovoltaic technologies such as dye-sensitized solar cells (DSSCs), Organic solar cells (OPV) and perovskite solar cells (PSCs).

<sup>a</sup> Univ. Grenoble Alpes, INAC-SPRAM, F-38000 Grenoble, France.

<sup>b</sup> CNRS, INAC-SPRAM, F-38000 Grenoble, France.

<sup>c</sup> CEA, INAC-SPRAM, F-38000 Grenoble, France.

<sup>d</sup> Department of Materials Science and Engineering, Korea Advanced Institute of Science and Technology (KAIST), 291 Daehak-ro, Yuseong-gu, Daejeon 34141, Republic of Korea. E-mail: idkim@kaist.ac.kr

See DOI: 10.1039/x0xx00000x



*Damien Joly obtained his Ph.D. in chemistry supervised by Prof. Muriel Hissler and Prof. Régis Réau from Rennes University in France, in 2010. From 2011 to 2012, he was a postdoctoral fellow in the Organic Chemistry Department at the Universidad Complutense in Madrid under the supervision of Prof. N.*

*Martin. In 2012 he joined as a post-doctoral fellow laboratory of molecular, hybrid and organic electronics at CEA Grenoble to develop organic sensitizers for solar cells. Since 2015, he is a temporary researcher in the same department. His research interests are mainly focused on the development of pi-conjugated materials for organic electronics and hybrid photovoltaics.*



*Prof. Il-Doo Kim received his Ph.D. degree in Materials Science and Engineering from Korea Advanced Institute of Science and Technology (KAIST). From 2003 to 2005, he was a postdoctoral fellow in Prof. Harry L. Tuller's group at Massachusetts Institute of Technology (MIT). He returned to Korea Institute of Science and Technology as a senior research scientist. He is now an*

*associate professor of the Department of Materials Science and Engineering at KAIST. His current research focuses on controlled processing and characterization of functional nanofibers via electrospinning for practical applications in exhaled breath sensors and Energy storage devices. He has published 148 articles and holds 157 patents. Prof. Kim is a Deputy Editor of the Journal of Electroceramics (Springer) and an associate member of the Korean Academy of Science and Technology.*

## 2. Electrospinning background and basic principles

### 2.1 Electrospinning process

Electrospinning is a kind of spinning on the basis of the use of electrostatic force. It has been employed as a powerful tool to produce high-quality organic and/or inorganic fibers, which reveal nanometer scale diameters and larger surface areas than the conventional fibers obtained from other spinning techniques such as melt-spinning and dry-spinning.<sup>20</sup> A schematic illustration for electrospinning and NF-synthetic process is shown in Fig. 1.



*Ji-Won Jung is currently a Ph.D. candidate in the research group of Prof. Il-Doo Kim in the Department of Materials Science and Engineering at Korea Advanced Institute of Science and Technology (KAIST). His major research interests focus on the field of electrode materials for advanced secondary batteries such as Li-ion batteries, Na-ion batteries and Li-air batteries.*



*Dr. Renaud Demadrille earned a degree in organic chemistry in 1997 and he received his Ph.D. in 2000 from the University of Aix-Marseille II with a grant from PPG Industries and Essilor International. After his PhD, he spent one year in the R&D center of an international chemical company and then he*

*joined the Atomic Energy Commission (CEA) as a postdoctoral fellow under the supervision of Prof. Adam Pron, before being appointed in 2005 as a permanent researcher in the laboratory of molecular, hybrid and organic electronics. His research focuses on the synthesis and the characterization of new pi-conjugated molecules and macromolecules for organic and hybrid photovoltaics. He is also interested in the development of new functional materials and nanomaterials for organic electronics. He has co-authored 55 articles and holds 5 patents.*

Fig. 1(a) shows a typical electrospinning set up, which basically is composed of three major parts: i) a small diameter-needle syringe including electrospinning solution (composed of a highly viscous polymer and various precursors (e.g. inorganic precursors), which are dissolved in solvents such as N,N-dimethylformamide (DMF), deionized (DI) water, N-Methyl-2-pyrrolidone (NMP) and ethanol etc.), ii) a high voltage power supplier, and iii) a grounded collector (usually conducting metallic plate). The nonwoven one-dimensional NFs are simply synthesized by applying a high voltage source (electric field) between a needle syringe tip and the grounded collector.

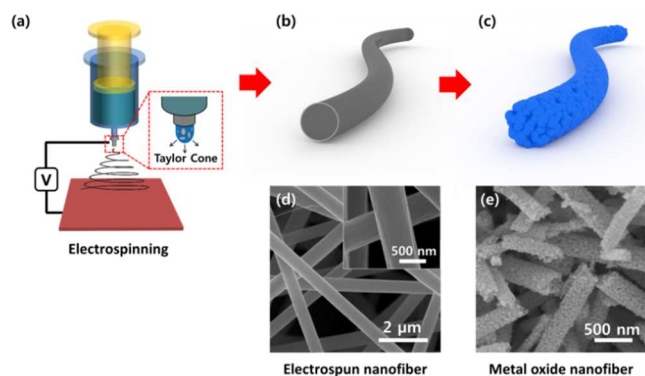


**Fig. 1** (a) Electrospinning equipment. (b) Inorganic precursor/polymer composite electrospun nanofiber ('as-spun nanofiber'). (c) Metal oxide nanofiber after high-temperature heat treatment in air atmosphere. (d-e) SEM images of the as-spun NFs and the metal oxide NFs corresponding to (b) and (c), respectively.

Firstly, the electrospinning solution is fed by a syringe pump, and an electric field is applied to induce electrified jet. During electrospinning, the hemispherical surface of the solution at the tip of the needle is electrically charged and continuously elongated to develop a cone-shape (referred to 'Taylor cone') with increasing the voltage.<sup>21</sup> When the applied electric field reaches sufficient value (over critical value), repulsive force between the charged surface and evaporation of solvent is larger than the surface tension of the solution.<sup>22</sup> A charged jet of the solution is then injected from the tip of the spinneret. Even though the jet is stable near to the end of the needle, the erupted solution goes through unstable elongation process and a rapid whipping of the jet arises in space between the capillary tip and collector. Meanwhile, a solvent is evaporated, and the precursors and/or polymer fibers are collected on ground plate in the form of nonwoven matrix. Fig. 1(b) shows the long and thin electrospun fibers (the so-called 'as-spun fibers') obtained by strong polymer template allowing the jet to be unbreakable. The as-spun fibers can be easily changed to metal oxide NFs by subsequent thermal treatment in air atmosphere, resulting in simultaneously removal of the matrix polymer and crystallite growth due to the oxidation of inorganic precursor (Fig. 1(c)). As an example, Fig. 1(d-e) show SEM images of as-spun Sn precursor/PVP composite fibers and SnO<sub>2</sub> NFs calcined at 500 °C for 2h, clearly revealing morphological change before and after high temperature calcination.

## 2.2 Parameters influencing electrospinning process

The electrospinning process is greatly influenced by several parameters, which can be categorized as follows:

- i) Operating parameters such as applied power voltage, the solution flow or feeding rate, a shape or gauge of needle, tip-to-collector distance
- ii) Solution parameters, such as the type of polymer matrix and solvent, solubility and viscosity of the solutions, molecular weight of the polymer, precursor type and their compatibility each other components<sup>23</sup>
- iii) Environmental parameters such as temperature and humidity.<sup>24</sup>

Through the optimized handling of these parameters, one can prepare NFs with desired morphology, microstructure, and composition. To illustrate this versatility, we show some examples of various morphological evolutions of the electrospun NFs as functions of processing parameters (Fig. 2). Fig. 2(a-c) show the morphologies and microstructures of electrospun TiO<sub>2</sub> fibers synthesized by using different polymers such as polystyrene (PS), poly(methyl methacrylate) (PMMA) and poly(vinyl acetate) (PVAc).<sup>25</sup> As shown in Fig. 2(a), TiO<sub>2</sub> NFs prepared by the removal of PS template are composed of TiO<sub>2</sub> nanoparticles (NPs) of ca. 30 nm, which is originated from fast phase separation driven by immiscibility between PS polymer and Ti precursors. PMMA has better miscibility with Ti-precursor than PS. This feature leads to the formation of smooth cladding surface layer, which is distinctly different with inner TiO<sub>2</sub> NPs (Fig. 2(b)). In the case of PVAc-driven TiO<sub>2</sub> fibers (Fig. 2(c)), the TiO<sub>2</sub> fibers showed fibrillar structure elongated along the fiber direction. It is important to note that the solidification of TiO<sub>2</sub> depends on the phase separation between selected polymers and Ti precursors. As a consequence, the phase separation in PS matrix occurs suddenly in the immiscible system, resulting in the formation of polycrystalline TiO<sub>2</sub> fibers consisted of small NPs. To the contrary, in the case of PVAc matrix, the phase separation slowly proceed, then Ti precursor-rich domains and PVAc-rich domains co-exist and allow the domains stretching in 1D direction during electrospinning process. After calcination, the PVAc matrix is removed, resulting in the formation of open pores while Ti precursor-rich domains are converted to TiO<sub>2</sub> phases. In parallel with polymer parameter, electrospinning solution feeding speeds (low, intermediate and fast flow rates) have significant effects on the morphology control of the NFs. For example, Fig. 2(d-f) show SEM and TEM images of as-spun fibers, calcined SnO<sub>2</sub> NFs at very high flow rate (25 μl/min).<sup>26</sup> When given fast injection rate, the solution jet was stretched in spinning direction. The large amount of solvent erupted from the end of the tip results in tremendous evaporation of solvent every moment, which allows unstable fluctuation of solution. The as-spun Sn precursor/PVAc composite fibers, as shown in Fig. 2(d), showed rough surface morphologies with elongated bumpy voids along the fiber direction. During heat-treatment, a number of furrows in the as-spun fibers were converted into elongated open holes at surface and inner part of the fibers. The small and large crevices indicated by blue arrows and dotted yellow frames in Fig. 2(d-f) are clear evidences for the effect of flow rate control assisted by the phase separation. In addition, facile synthesis of core-shell, multi-walled tubular and multichannel structures via an electrospinning route has been successfully demonstrated (Fig. 2(g-i)). Fig. 2(g) shows SEM image of a coaxial bundle of anatase TiO<sub>2</sub> hollow NFs prepared by dual-nozzle electrospinning.<sup>27</sup> In a typical procedure, a spinneret including two viscous and immiscible solutions is simultaneously fed through two co-axial capillaries.

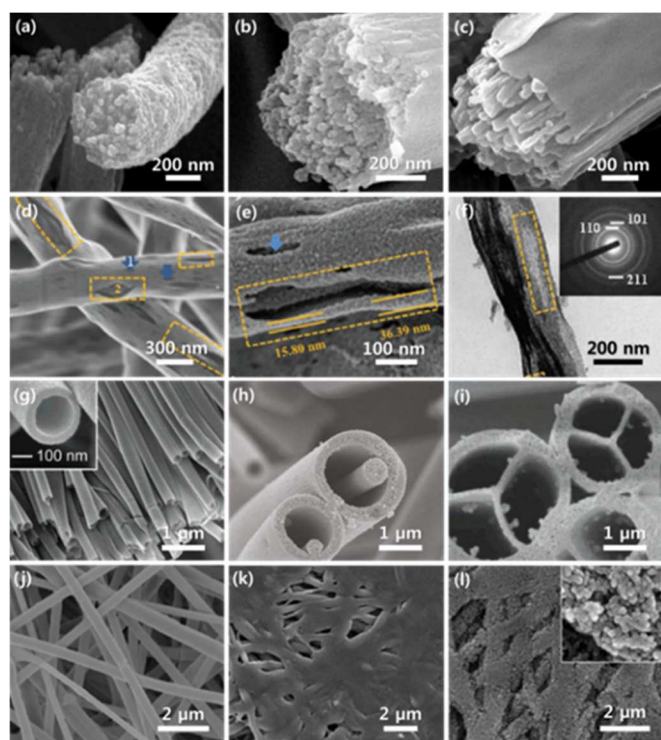


**Fig. 2** The SEM images show the morphologies of electrospun NFs, depending on various parameters such as (a-c) different kind of polymers; (d-f) solution feeding rate; (g-i) the shape of needle; (j-l) pressing. The (a-c) shows the SEM images of TiO<sub>2</sub> NFs prepared from (a) PS, (b) PMMA and (c) PVAc (Reproduced with permission from ref [25]. Copyright 2005 Taylor & Francis Group). The (d-f) shows SEM image of (d) as-spun Sn precursors/PVAc composite fibers, (e) SEM image and (f) TEM image of calcined SnO<sub>2</sub> NFs at the high feeding rate (Reproduced with permission from ref [26]. Copyright 2013 Wiley). The (g-i) shows SEM images of TiO<sub>2</sub> NFs synthesized via (g) dual-nozzle (Reproduced with permission from ref [27]. Copyright 2004 American Chemical Society), (h) triple-nozzle (Reproduced with permission from ref [28]. Copyright 2010 American Chemical Society) and (i) Y-shape inner ridge nozzle (Reproduced with permission from ref [29]. Copyright 2007 American Chemical Society). The (j-k) shows the SEM images of the as-spun fibers of Ti precursors/PVAc composite (j) before and (k) after hot-pressing, and the (l) shows the SEM image of hot-pressed TiO<sub>2</sub> nanofiber after calcinations at 450 °C (Reproduced with permission from ref [30]. Copyright 2006 American Chemical Society).

The matrix polymer in the core and shell is eliminated, and Ti-precursor loaded in only matrix shell undergoes oxidation and crystallization to form crystalline TiO<sub>2</sub> fibers during calcination. In similar way (the so-called ‘multi-fluidic coaxial electrospinning’), independent TiO<sub>2</sub> nanofiber (Fig. 2(h))<sup>28</sup> and Y-shaped TiO<sub>2</sub> nanofiber (Fig. 2(i)),<sup>29</sup> which are embedded in the center of TiO<sub>2</sub> microtubes, were also synthesized. In order to improve the adhesion strength between fibers mats and underlying substrates, thermo-compression step was introduced prior to the calcination step. Fig. 2(j-l) show the morphological difference between as-spun fibers and hot-pressed fibers.<sup>30</sup> The as-spun fibers without hot-pressing treatment exhibit typical nanofiber mats (Fig. 2(j)), on the other hand, hot-pressed fibers show interconnected network structure due to the partial melting of PVAc matrix polymer with low glass transition temperature (Fig. 2(k)). Subsequently, after calcination step at 450 °C for 30 min, highly porous TiO<sub>2</sub> NFs composed of single crystalline anatase nanorods (NRs) are achieved (Fig. 2(l)).

### 3. Electrospun materials for DSSCs

Dye-sensitized solar cells (DSSCs) are photo-electrochemical devices capable to convert solar radiation directly into electricity. Basically, they consist in a photoanode and a counter electrode separated by an electrolyte that can be a liquid or an ionic liquid containing a redox couple. Alternatively, a hole transporting material (HTM) can be used to replace the liquid element. The breakthrough in the photon to electron conversion efficiency of DSSCs was achieved in the early 1990s when Grätzel and O’Regan used a colloidal TiO<sub>2</sub> film to fabricate a mesoporous photoanode in replacement of bulk materials employed so far.<sup>31,32</sup> Since this discovery, DSSCs have attracted considerable interest due to their low cost fabrication process, their short energy payback time and their relatively high conversion efficiency and stability.<sup>33</sup> Besides, this technology is compatible with large area surfaces, and in the last years industrial developments have successfully demonstrated its potential for building integrated photovoltaics (BIPV).<sup>34,35</sup>

In a typical DSSC, the photoanode is composed by a transparent conducting oxide (TCO) coated with a nanostructured film of a wide band gap metal oxide semiconductor. The counter electrode usually employed is a TCO coated with a thin layer of platinum. In these devices light is absorbed by a photo-sensitizer attached to the metal oxide surface through an anchoring function. Upon irradiation, the electrons are injected from the excited state of the dye into the conduction band of the semiconductor and transported to the counter electrode through an external circuit. In the meantime the oxidized dye is regenerated thanks to the redox system present in the electrolyte which is itself reduced at the counter electrode. The detailed description of the basic working principles can be found elsewhere.<sup>36,37</sup>

Among the fruitful strategies to improve the performances of DSSCs, one consists in increasing the short-circuit current density (J<sub>sc</sub>) delivered by the solar cells by improving the light harvesting efficiency of the photoanodes. On one hand, this can be achieved by synthesizing new sensitizers showing a higher molar absorption coefficient and revealing absorption domains better matching the solar emission spectrum.<sup>38</sup> On the other hand, this goal can also be achieved by developing nanostructured electrode materials presenting light scattering properties and showing dramatically enhanced specific surface areas, in order to increase the number of dye molecules that can bind to the surface.<sup>39</sup>

One should keep in mind also that, in DSSCs, the open circuit photovoltage (V<sub>oc</sub>) is given by the difference of the Fermi level of electrons in the metal oxide and the redox potential of the electrolyte. Therefore by tuning the chemical composition of the photoanode materials (by employing various metals and doping elements) it is possible to adapt the Fermi level of the semiconductor and to increase the V<sub>oc</sub> of the solar cells. These strategies based on the fine tuning of the electrode materials have initially sparked the strong interest of materials scientists for integrating electrospun components into photovoltaic devices.

### 3.1 Electrospun materials as photoanodes in DSSC

#### 3.1.1 TiO<sub>2</sub> photoanodes prepared by electrospinning.

Screen-printing coating of TiO<sub>2</sub> NPs is the most popular and convenient technique to prepare the mesoporous thin films that are utilized as photoanodes in DSSCs. Typical TiO<sub>2</sub> mesoporous layers show thickness in the range of 2 - 16  $\mu\text{m}$  and are made of colloidal NPs with diameters of 15 to 40 nm. In most cases, the particles are prepared from controlled sol-gel hydrolysis of titanium alkoxides. In these layers the surface states influence strongly the photo-induced charge transfer that occurs between the sensitizer and the metal oxide and the connectivity between the particles greatly influences the transport of free electrons through the mesoporous nanoparticle network.

Recently one-dimensional (1D) TiO<sub>2</sub> nanostructures such as nanotubes (NTs)<sup>40</sup> or nanorods (NRs)<sup>41</sup> have attracted interest for the fabrication of DSSC with either liquid or quasi solid-state electrolytes. Indeed, the devices based on the 1D nanostructures demonstrated higher photocurrent generation compared to conventional NPs-based systems. This improvement was attributed to the reduced grain boundaries with 1D structures compared to those of the sintered NPs. One of the first examples of the use of electrospinning technique for the preparation of photoanode with 1D nanostructures was reported by Song *et al.* in 2004.<sup>42</sup> In this pioneer work, authors faced difficulties to ensure adhesion of the TiO<sub>2</sub> NFs on the conductive glass. Adhesion of the NFs produced from electrospinning is a general problem and several strategies have been developed to solve it. In particular, Song *et al.* have pre-treated NFs prior to calcination with solvent vapour (THF) in order to partially melt the polymer matrix in which the inorganic precursors are embedded with the goal to promote interconnection of the fibers. After heat treatment fibers made of anatase crystallites were formed and the TiO<sub>2</sub> web electrodes maintained their porous structure and showed a better adhesion on the substrate. The resulting photoanodes were subsequently treated with TiCl<sub>4</sub> that contributed to a dramatic increase of the current density up to 11.24 mA.cm<sup>-2</sup> and to boost the power conversion efficiency (PCE) up to 5% for the solar cells (Table 1).

Alternatively to a vapour exposure treatment, Onozuka *et al.* reinforced the adhesion between fibers and substrates by dipping for a short period the as-spun fibers in DMF which a poor solvent for PVAc employed in this case as sacrificial template.<sup>39</sup> After the calcination step, the NFs made of anatase TiO<sub>2</sub> crystallites, as revealed by XRD patterns, showed a good adhesion with the pre-deposited dense layer of TiO<sub>2</sub>. Different thicknesses of TiO<sub>2</sub> fibers were investigated and the highest efficiency for the corresponding solar cells reached 4.14% for a 3.9  $\mu\text{m}$  thick electrode. In addition to solvent treatments, more recently Du *et al.* demonstrated that the TiCl<sub>4</sub> treatment also reinforces the strength and adhesion of the TiO<sub>2</sub> NFs films.<sup>43</sup> Single-crystalline NRs of TiO<sub>2</sub> have also been prepared from electrospun NFs and similar adhesion difficulties were encountered.<sup>41</sup> Herein, alternatively to solvent treatments, a mechanical hot-pressing step was employed to ensure adhesion of the as-spun Ti precursor/PVAc composite fibers with the FTO. Upon this kind of treatment, each fibril gave rise to NRs which were converted

to anatase single crystals after calcination. A DSSC was fabricated using these TiO<sub>2</sub> NRs electrodes sensitized with a ruthenium dye (N3), and a gel-based electrolyte (PVDF-HFP) was used instead of a liquid electrolyte. An efficient penetration of the highly viscous gel electrolyte into the TiO<sub>2</sub> electrode was observed through large pores in the web. The well-aligned 1D TiO<sub>2</sub> NRs and the good penetration of gel ensured a high J<sub>sc</sub> of 14.77 mA.cm<sup>-2</sup> for the resulting quasi solid-state solar cells leading to a rather good power conversion efficiency of 6.2% (Table 1).

While controlling finely this mechanical hot-pressing step, during the calcination process Hwang *et al.* were capable to obtain highly porous fiber-based photoanode with large pore volume of *circa* 2.41 m<sup>3</sup>.g<sup>-1</sup>, and large surface area of 112 m<sup>2</sup>.g<sup>-1</sup>.<sup>44</sup> It was therefore appealing to use them in quasi-solid state and solid-state DSSC configuration where the penetration of the hole transporting material is often problematic. Using these hierarchically structured TiO<sub>2</sub> NFs with large pores, efficiency of solar cells reached 6.54%. This improvement was attributed to a better pore filling by the plastic crystal-based solid-state electrolytes that lowered series resistance and improved charge collection (Table 1).

In 2009, the efficiency of electrospun TiO<sub>2</sub> NR photoelectrodes was greatly improved to reach 9.52%.<sup>45</sup> This impressive value is still the efficiency record for non-doped electrospun materials. The optimization in the sol-gel chemistry and electrospinning process led to fibers constituted of NRs structures with diameters of *circa* 15 nm and lengths of 60-100 nm. These NR fibers allowed the preparation of electrodes showing higher active surface area and larger pore volume than classical fibers. To increase further the surface area of the electrodes, Hwang *et al.* developed a template approach with SiO<sub>2</sub> NPs.<sup>46</sup> TiO<sub>2</sub> NFs were fabricated by a simple electrospinning method starting from mixed solution containing the precursors together with colloidal SiO<sub>2</sub>. Etching step with an HF solution allowed to create wormhole-like pores in the TiO<sub>2</sub> NFs. These large pores facilitate electrolyte diffusion for oxidation reactions (regeneration of the dyes) and also contribute to a higher dye loading. Actually the surface area of this electrospun photoanodes was found nine times higher than the usual pristine TiO<sub>2</sub>-based photoanode. Following this strategy a rather high PCE of 8.50% was reached for the solar cells (Table 1). A similar approach was developed by Nair *et al.* but in this work the etching of SiO<sub>2</sub> from electrospun TiO<sub>2</sub>-SiO<sub>2</sub> composite was carried out using NaOH. The performances of the resulting solar cells were slightly above 7% in this case (Table 1).<sup>47</sup> To fabricate 1D mesoporous TiO<sub>2</sub> NFs with wormhole-like pores, Lin *et al.* developed a simple electrospinning method combined with a sol-gel process in which they used a small fraction of room-temperature ionic liquid as the mesopore formation template.<sup>48</sup> The porosity of the NFs was tuned by varying the amount of ionic liquid content in the feeding solution during the electrospinning process. The ionic liquid entrapped in the fibers was subsequently removed by washing it with anhydrous ethanol before their calcination. After this step, highly porous NFs with surface area up to 90 m<sup>2</sup>.g<sup>-1</sup> were obtained. Using these NFs, efficiency up to 5.64% was reached compared to 3.75% without

the use of ionic liquid (Table 1). Alternatively to ionic liquids, paraffin oil microemulsion droplets were also tested as the soft template for the preparation of electrospun NFs to form multiscale ultraporos NRs.<sup>49</sup> TiO<sub>2</sub> NRs with a composite structure of mesopores and macropores were prepared following this procedure. Subsequently, they were formulated as pastes and deposited by screen-printing. The efficiency of DSSC based on these NRs as photonode was lower than the one of conventional NPs mainly because they showed a lower active surface area (Table 1). However when the material was employed as scattering layer on top of NPs the conversion efficiency was enhanced up to 8.53%.

More commonly the template role is played directly by the polymers employed in the starting solution. Several groups have reported that when the polyvinyl pyrrolidone (PVP) matrix is swapped to polyvinyl acetate (PVAc) or to a mixture of PVP and PVAc, the morphology of the TiO<sub>2</sub> varies from continuous fibers to rice-shaped<sup>50,51</sup> and to leaf-shaped<sup>52</sup> nanostructures. Indeed, the nature of the matrix has a strong impact on the structural characteristics of the final NFs such as surface area, crystallinity and shapes and ultimately it impacts the photovoltaic properties (Table 1).<sup>53</sup> To increase the active surface area of NFs Koo *et al.* recently developed a co-electrospinning technique involving PVPs of different molecular weights.<sup>54</sup> The TiO<sub>2</sub> nanowires (NWs) prepared from different molecular weight fractions of PVP showed higher surface area and a roughened aspect compared to NWs prepared from a single fraction (67.65 m<sup>2</sup>·g<sup>-1</sup> against 23.93 m<sup>2</sup>·g<sup>-1</sup>). A clear effect on the dye loading was evidenced, but despite of improving this parameter, the PCE of the corresponding solar cells remained below 4% (Table 1). Zhang *et al.* demonstrated that when two non-miscible polymers are employed such as PVP and polyethylene oxide (PEO) it is possible to obtain core-shell nanostructures (see Fig. 3) where TiO<sub>2</sub>-PVP blend covers a PEO core nanofiber.<sup>55</sup> After calcination, hollow NFs were obtained with superior characteristics in terms of surface area and pore volume compared to the classical NFs. Devices fabricated with the hollow NFs exhibit higher J<sub>sc</sub> and V<sub>oc</sub> due to higher dye loading and better electrolyte penetration in the mesopores of the films compared to conventional NFs. To synthesize similar hollow nanostructures Wang *et al.* developed a coaxial electrospinning procedure.<sup>56</sup> Instead of PEO, paraffin oil was employed as sacrificial template. A syringe containing paraffin oil was connected to the inner capillary of the spinneret containing the Ti precursor and PVP solution. After calcination, NTs with inner diameter of *circa* 275 nm and wall thickness of around 115 nm were obtained. These nanostructures showed an anatase-type crystalline phase. The device performances comprising them were limited (around 4.3%) because of a lower dye loading compared to a classical NPs-based photoanode. Nevertheless this drawback was partially overcome by a faster electron transport in the NTs which improves charges collection and gives rise to a longer electron lifetime, leading to higher V<sub>oc</sub>.

Template-assisted synthesis was also demonstrated with an amphiphilic triblock copolymer as the structure directing agent.<sup>57</sup> With this strategy photoanodes with a surface area of 112 m<sup>2</sup>·g<sup>-1</sup> and rather large pores, 6 ± 0.5 nm were fabricated. The large size

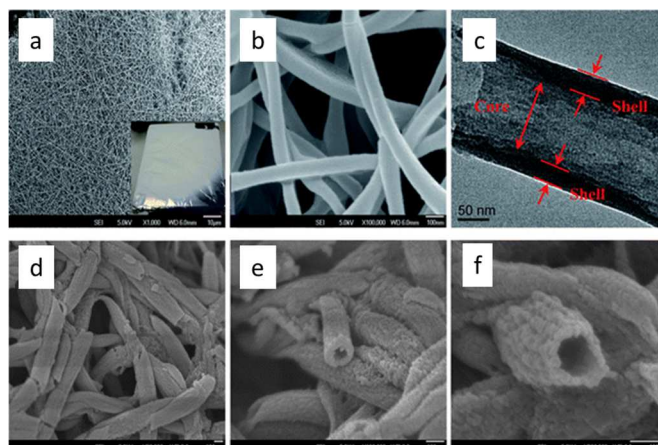


**Fig. 3** (a) SEM image of a bundle of core-shell (PEO/TiO<sub>2</sub>-PVP) composite nanofibers. [The inset is the photo of core-shell (PEO/TiO<sub>2</sub>-PVP) composite nanofibers samples.]. (b) Close-up image of a bundle of core-shell (PEO/TiO<sub>2</sub>-PVP) composite nanofibers. (c) TEM image of core-shell (PEO/TiO<sub>2</sub>-PVP) composite nanofibers. (d) SEM image of a bundle of hollow mesoporous TiO<sub>2</sub> nanofibers. (e) Close-up tilted view image of a bundle of hollow mesoporous fibers TiO<sub>2</sub>. (f) Close-up image of one single hollow mesoporous TiO<sub>2</sub> nanofibers. Reproduced with permission from ref [55]. Copyright 2012 The Royal Society of Chemistry.

of the pores enabled the use of P3HT as the hole transporting material. Solid state DSSC were fabricated from the NFs synthesised with or without template. In this work the TiO<sub>2</sub> was sensitized with an organic dye (D131) and the resulting PCE was 4 times higher compared to the mesoporous NFs prepared *via* the template-assisted method. The larger J<sub>sc</sub> attained in this case was attributed to a higher dye loading and a better pore filling with the HTM (Table 1).

Apart of the composition of the initial Ti-precursor/polymer blend, the effect of critical parameters such as feeding rate during the electrospinning process or temperature during calcination step were investigated. It was clearly evidenced that the temperature of the calcination step plays a crucial role in the formation of different structures. This was illustrated by several teams and notably Kumar *et al.* who annealed their fibers prepared from Ti precursor and PVAc at different temperatures ranging from 400 °C to 800 °C.<sup>58</sup> Varying the growth conditions, pure anatase, mixed, and pure rutile TiO<sub>2</sub> phases were obtained. The transformation of regular fibers to porous rod/hollow tube structure, and to spindle network structures was influenced by polymer degradation and crystallite reformation processes. The variations of shape and crystallinity resulted in photovoltaic performances spanning from 0.79% to 4.56% (Table 1). The critical effect of the calcination temperature was also highlighted by Lin *et al.* who developed a template-free alkali hydrothermal route to synthesize NFs.<sup>59</sup> A prickle-like structure was formed by controlling precisely the parameters of the calcination step. When this step is performed at 150 °C for 12 h prickle-like branches grow off the TiO<sub>2</sub> nanofiber backbone leading to significantly larger surface area (154 m<sup>2</sup>·g<sup>-1</sup>) than conventional

fibers ( $36 \text{ m}^2 \cdot \text{g}^{-1}$ ). After optimization of the device fabrication, PCE of *circa* 7.9% was achieved using the prickly-like nanostructures. The influence of the feeding rate during the electrospinning process was investigated as well. Mali *et al.* prepared NFs with different diameters by varying the feeding rate during the deposition.<sup>60</sup> At low feeding rate *i.e.*  $1.0 \text{ mL} \cdot \text{h}^{-1}$ , thin fibers (296 nm wide) were formed whereas for higher feeding rate *i.e.*  $2.5 \text{ mL} \cdot \text{h}^{-1}$  wider fibers (639 nm wide) were obtained. Bigger fibers do not necessarily lead to greater active surface area as it was evidenced in this work. Indeed the NFs deposited at  $1.5 \text{ mL} \cdot \text{h}^{-1}$  (421 nm) showed highest efficiency at 5.39%, this performance was attributed to a higher dye loading related to a higher surface area ( $147.8 \text{ m}^2 \cdot \text{g}^{-1}$ ) (Table 1).

After analysing in details literature, it turns out that NFs offer better charge transport properties but the device performances remain very often lower than the ones obtained for devices based on NPs. Several groups tried to take advantages of both nanostructures by combining NPs and NFs. In 2008, Chuangchote *et al.* electrospun NFs layer of  $1 \mu\text{m}$  thick on top of a  $\text{TiO}_2$  NPs-based photoanode.<sup>61</sup> The  $J_{\text{sc}}$  of the NFs-containing cells was found to be higher compared to the ones containing solely NPs (Table 1). Authors attributed this effect to improved charge transport properties in these electrodes but also to a light scattering effect originating from the NFs layer. Similar property was observed by Lee *et al.* who used different thicknesses of electrospun NFs on top of NPs (Table 1).<sup>62</sup> With the same philosophy, Zhu *et al.* prepared nest-shaped NPs by electrospinning to act as a scattering layer (Fig. 4).<sup>63</sup> The photocurrent of DSSCs containing the nest-shaped NPs was relatively high due to the improvement of light harvesting and lower electron transfer resistance (Table 1). This resulted in relatively high efficiency of 8.02%.

Joshi *et al.* proposed a different strategy and synthesized nanoparticles (NPs)/nanofibers (NFs) composite by dispersing various amount of electrospun NFs in conventional  $\text{TiO}_2$  NPs.<sup>64</sup> Their study revealed that the presence of electrospun  $\text{TiO}_2$  NFs noticeably improves the management of light in the active layer through scattering effect without substantially sacrificing the dye uptake. A PCE of 8.8% was obtained with such electrodes. (1D) assembly of  $\text{TiO}_2$  NPs was also investigated as scattering layer. Indeed Gao *et al.* prepared a blends of conventional  $\text{TiO}_2$  NPs and PVP dispersed in ethanol and used it as electrospinning precursor solution. Their work showed that the 1D assembly of NPs can enhance simultaneously electron transport and light scattering (Table 1).<sup>65</sup> A similar effect was recently demonstrated using electrospun  $\text{TiO}_2$  NRs constituted of NPs.<sup>66,67</sup> To take advantage of light scattering and of a large surface area, Yang *et al.* prepared photoanodes consisting of two layers of electrospun  $\text{TiO}_2$  NFs showing different diameters, respectively 60 and 100 nm.<sup>68</sup> For this device architecture, it was demonstrated that the smaller-diameter nanofiber layer, with a large surface can adsorb a large quantity of dyes. As a result this layer efficiently harvests sunlight and transport photo-generated electrons, on the other hand the bigger-diameter nanofiber layer reflects and traps sunlight in the photoanode. The PCE of this type of DSSC can be increased up to 8.4%.

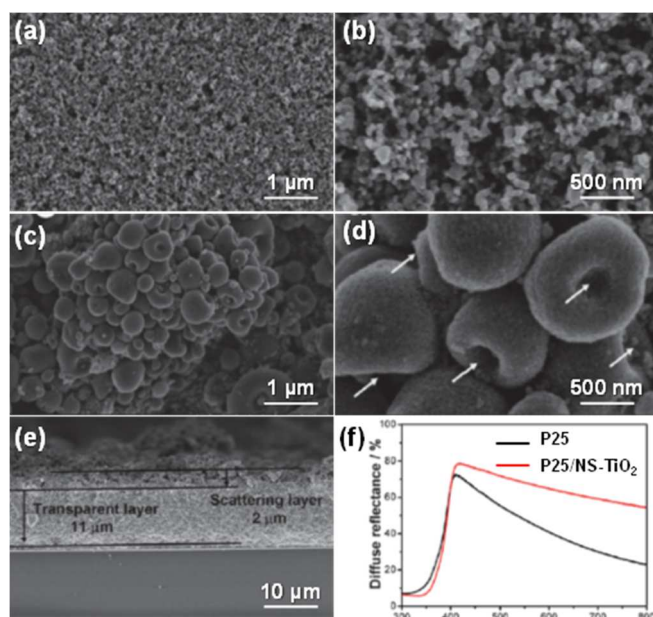


**Fig. 4** Surface morphologies of (a) P25 and (c) P25/NS- $\text{TiO}_2$  electrodes; Fig. 4. Surface morphologies of (a) P25 and (c) P25/NS- $\text{TiO}_2$  electrodes; (b) and (d) are corresponding magnified FESEM images; (e) cross-sectional FESEM image of the as-prepared P25/NS- $\text{TiO}_2$  electrode, and (f) UV-vis diffuse reflectance spectra of P25 and P25/NS- $\text{TiO}_2$  electrodes. Reproduced with permission from ref [63]. Copyright 2012 The Royal Society of Chemistry.

The scattering effect of electrospun materials revealing various shapes was investigated in details by Zhu *et al.* who synthesized and compared rice grain- or nanofiber-shaped  $\text{TiO}_2$ .<sup>69</sup> Both type of nanomaterials showed similar diameter and surface area. To compare their scattering ability,  $2 \mu\text{m}$  thick layer of these materials were deposited on top of a  $10 \mu\text{m}$  thick layer of conventional  $\text{TiO}_2$  NPs. Photovoltaic parameters of the devices showed that the both  $J_{\text{sc}}$  and  $V_{\text{oc}}$  of rice-grain shape  $\text{TiO}_2$ -based device were higher (Table 1). The enhancement of  $J_{\text{sc}}$  was attributed to a better light scattering effect while the improvement of  $V_{\text{oc}}$  was attributed to reduced grain boundaries leading to lower recombination rate. These features are particularly interesting for increasing the  $J_{\text{sc}}$  in solar cells. Several groups have demonstrated that 1D nanostructures generally show reduced grain boundaries that plays an important role on the recombination processes allowing to improve simultaneously  $J_{\text{sc}}$  and  $V_{\text{oc}}$ .

This brief overview illustrates that electrospinning can lead to a large structural diversity of  $\text{TiO}_2$  nanostructures by simply tuning the chemical composition of the precursors solution or relevant processing parameters such as the calcination temperature or the mechanical hot-pressing etc. Electrospun  $\text{TiO}_2$  materials can be deposited directly on the substrates, or they can be formulated as printable pastes.<sup>70</sup> Moreover, following appropriate procedures, they can even be vertically aligned perpendicular to the substrate.<sup>71</sup>



## Journal of Materials Chemistry C

## ARTICLE

**Table 1:** photovoltaic parameters of DSSC using electrospun photoanode

TiO <sub>2</sub> photoanodes prepared by electrospinning	J <sub>sc</sub> [mA·cm <sup>-2</sup> ]	V <sub>oc</sub> [V]	FF [%]	η [%]	Comments	Ref.
NR (12 μm)	14.77	0.70	60	6.20	N3 dye, polymer gel	41
NF (no TiCl <sub>4</sub> treatment) (20 μm)	8.67	0.77	60	4.01	N3 dye	42
NF (no TiCl <sub>4</sub> treatment) (20 μm)	8.07	0.80	59	3.80	N3 dye, polymer gel	
NF (TiCl <sub>4</sub> treatment) (20 μm)	11.24	0.77	58	5.02	N3 dye	
NF (TiCl <sub>4</sub> treatment) (20 μm)	10.52	0.78	56	4.60	N3 dye, polymer gel	
NF (2 μm) no DMF treatment	4.99	0.82	45	1.86	N3 dye	39
NF (2 μm)	6.26	0.81	49	2.50	N3 dye	
NF (3.9 μm)	9.88	0.82	51	4.14	N3 dye	
NF (3 μm) on NP (no TiCl <sub>4</sub> post-treatment) (3 μm)	10.60	0.70	60	4.46	N719	43
NF (3 μm) on NP (TiCl <sub>4</sub> post-treatment) (3 μm)	12.20	0.73	61	5.40	N719	
NF (9 μm)	11.30	0.67	71	5.41	N719, plastic crystal	44
NF (14 μm)	14.10	0.67	69	6.54	N719, plastic crystal	
Reference TiO <sub>2</sub> NP (9 μm)	7.10	0.60	62	2.65	N719, plastic crystal	
NR (14 μm)	17.60	0.761	70	9.52	N719	45
NF	10.70	0.71	62	4.8	N719	46
Large pores NF	12.60	0.72	65	6.0	N719	
Small pores NF	15.60	0.72	68	7.6	N719	
Multiscale pores NF	16.30	0.73	71	8.5	N719	
Reference NP	12.00	0.71	70	6.0	N719	
NF after SiO <sub>2</sub> etching	14.38	0.75	65	7.02	N3 dye	47
NF of "rice grain" after SiO <sub>2</sub> etching	14.12	0.74	64	6.72	N3 dye	
NF	8.60	0.75	58	3.75	N719	48
NF (1 wt.% of template)	13.70	0.73	56	5.64	N719	
NF (2 wt.% of template)	13.00	0.72	59	5.50	N719	
NF (3 wt.% of template)	11.70	0.71	53	4.45	N719	
NR (15 μm)	11.16	0.81	67	6.07	N719	49
NP (15 μm)	13.65	0.79	66	7.11	N719	
NP + NR (20 μm)	16.19	0.78	68	8.53	N719	
Reference TiO <sub>2</sub> NP (20 μm)	14.73	0.78	68	7.79	N719	
TiO <sub>2</sub> NF "rice grain" (12 μm)	8.2	0.96	62	5.1	N3	50
TiO <sub>2</sub> NF "rice grain" (11 μm)	9.40	0.815	60	4.63	N3	51
Reference TiO <sub>2</sub> NP (11 μm)	9.34	0.765	62	4.49	N3	
NP: 15% NF (PVP, calcinated at 500 °C) (2.2 μm)	9.0	0.63	77	4.31	C106	53
NP: 15% NF (PVP, calcinated at 590 °C) (2.2 μm)	8.7	0.62	75	4.11	C106	
NP: 15% NF (HPC, calcinated at 500 °C) (2.2 μm)	9.9	0.64	76	4.65	C106	
NP (2.2 μm)	11.0	0.65	70	4.96	C106	
"Roughened" TiO <sub>2</sub> NW	8.94	0.67	59.89	3.63	N719	54

Conventional TiO <sub>2</sub> NW	5.88	0.67	59.23	2.36	N719	
Hollow NF (12 μm)	10.38	0.76	72	5.61	N719	55
NF (12 μm)	8.99	0.74	64	4.17	N719	
TiO <sub>2</sub> NT (18 μm)	6.01	0.80	69	3.33	N719	56
NT/NP (8/2) (18 μm)	7.91	0.78	69	4.26	N719	
Reference TiO <sub>2</sub> NP (11 μm)	11.50	0.74	70	5.98	N719	
NF (1.8 μm)	0.97	0.86	50	0.42	D131, solid state (P3HT)	57
Mesoporous NF (1.8 μm)	3.98	0.92	50	1.82	D131, solid state (P3HT)	
Spindle (annealed at 400 °C) (20 μm)	1.98	0.77	52	0.79	N719	58
Porous rod (annealed at 500 °C) (20 μm)	8.61	0.80	66	4.56	N719	
Rod structure (annealed at 600 °C) (20 μm)	4.55	0.78	69	2.47	N719	
Hollow tube (annealed at 700 °C) (20 μm)	3.79	0.80	71	2.16	N719	
Spindle network (annealed at 800 °C) (20 μm)	2.18	0.83	64	1.17	N719	
NF (20 μm)	8.6	0.76	63	4.09	N719	59
Hierarchical NF (20 μm)	9.2	0.75	58	3.98	N719	
NP (6 μm) + NF (14 μm)	13.5	0.75	62	6.24	N719	
NP (6 μm) + hierarchical NF (14 μm)	16.2	0.75	65	7.86	N719	
Reference TiO <sub>2</sub> NP (20 μm)	10.9	0.73	63	4.98	N719	
NF (speeding rate 1 mL.h <sup>-1</sup> )	8.62	0.719	63	4.09	N719	60
NF (speeding rate 1.5 mL.h <sup>-1</sup> )	13.32	0.698	55	5.39	N719	
NF (speeding rate 2.5 mL.h <sup>-1</sup> )	10.21	0.694	61	4.55	N719	
Reference TiO <sub>2</sub> NP	8.61	0.718	60	3.96	N719	
TiO <sub>2</sub> NF/NP (8,4 μm)	15.90	0.71	68	7.10	N719	61
TiO <sub>2</sub> NP (8,4 μm)	14.00	0.7	68	6.69	N719	
TiO <sub>2</sub> NF/NP (15,5 μm)	17.90	0.69	66	8.14	N719	
Reference TiO <sub>2</sub> NP (15,5 μm)	16.10	0.69	67	7.47	N719	
Reference TiO <sub>2</sub> NP (6 μm)/NF (6 μm)	5.11	0.72	72	2.69	N719	62
Reference TiO <sub>2</sub> NP (8 μm)/NF (4 μm)	8.05	0.71	69	3.94	N719	
Reference TiO <sub>2</sub> N (10 μm)P/NF (2 μm)	8.92	0.70	67	4.21	N719	
Reference TiO <sub>2</sub> NP (12 μm)	5.84	0.74	71	3.16	N719	
NP (11 μm) + nestshape NP (2 μm)	14.29	0.79	71	8.02	N719	63
NP (11 μm) + reference NP scattering layer (2 μm)	14.10	0.79	70	7.83	N719	
Reference TiO <sub>2</sub> NP (13 μm)	13.41	0.79	71	7.49	N719	
NF (7.5 μm)	5.7	0.81	63	2.9	N719	64
NF/NP (15%) (7.5 μm)	16.8	0.82	64	8.8	N719	
Reference TiO <sub>2</sub> NP (7.5 μm)	11.4	0.77	70	6.1	N719	
Assembly NP (12 μm)	11.19	0.65	71	5.19	N719	65
NP (6 μm) + assembly NP (6 μm)	16.54	0.64	64	6.85	N719	
Reference TiO <sub>2</sub> NP (12 μm)	14.07	0.61	70	5.96	N719	
NP (15 μm)	10.30	0.630	68	4.68	N719	66
NR (15 μm)	8.55	0.725	69	4.30	N719	
NP (12 μm) + NR (3 μm)	16.02	0.635	69	6.60	N719	
NP (9 μm) + NR (6 μm)	14.72	0.640	69	6.49	N719	
NP (6 μm) + NR (9 μm)	14.83	0.635	68	6.50	N719	
NP (3 μm) + NR (12 μm)	11.94	0.695	69	5.74	N719	
NP	12.9	0.707	69	6.37	N719	67
NR	11.4	0.648	66	4.92	N719	

NP+NR	15.7	0.710	72	8.03	N719	
Single layer (small NF, 5.5 $\mu\text{m}$ )	6.5	0.67	52	2.50	N719	68
Single layer (small NF, 9.2 $\mu\text{m}$ )	20.1	0.74	48	7.14	N719	
Bilayer (small NF + big NF, 5.4 $\mu\text{m}$ )	9.6	0.72	63	4.30	N719	
Bilayer (small NF+ big NF, 8.9 $\mu\text{m}$ )	22.5	0.71	60	8.40	N719	
NP (10 $\mu\text{m}$ ) + NF (2 $\mu\text{m}$ )	14.9	0.74	64	7.06	N3 Dye	69
NP (10 $\mu\text{m}$ ) + NF "rice grain" (2 $\mu\text{m}$ )	15.7	0.74	64	7.45	N3 Dye	
Reference TiO <sub>2</sub> NP (12 $\mu\text{m}$ )	13.6	0.72	66	6.44	N3 Dye	
NR (12 $\mu\text{m}$ )	8.00	0.81	62	4.02	N3	70
TiO <sub>2</sub> NF "vertical"	5.71	0.78	64	2.87	N719	71

NF: nanofibers, NP: nanoparticles, NR : nanorods, NS: nanosheet, NT: nanotubes, NW: nanowires, liquid electrolyte unless stated otherwise.

### 3.1.2 Electrospun TiO<sub>2</sub> doped or coated with metals.

Another strong advantage of electrospinning relies on the possibility to tune very easily the chemical structure and the crystallinity of the final nanostructures by simply adjusting the composition of the precursor's solution (polymer matrix and metal precursor components). Complex chemical compositions including various nanostructures can be obtained. Examples of such heterostructures include TiO<sub>2</sub>-Al<sub>2</sub>O<sub>3</sub> NFs or TiO<sub>2</sub> doped with various metals.<sup>72,73,74,75</sup> An interesting approach in photovoltaics consists in using Au or Ag nanostructures in the photo-active layer in order to take benefit from surface plasmonic effect to enhance absorption.

Naphade *et al.* explored this concept and prepared electrospun NFs from titanium and gold precursors mixed in PVP.<sup>73</sup> After the calcination step the presence of tiny Au NPs dispersed uniformly in the semiconducting oxide matrix was evidenced by TEM and EDAX analysis. The Au content was close to 1 wt.% in the TiO<sub>2</sub> NFs and the size of the NPs was in the range of 5 to 10 nm (Fig. 5). Those Au-doped TiO<sub>2</sub> NFs were used in the scattering layer of a DSSC device. It was showed that Au loaded fibers help improving mainly the current density and the fill factor of the devices. This was attributed to better light harvesting properties of the doped fibers tentatively attributed to plasmon-polariton modes and to a lower charge recombination attributed to nanoscale Schottky junctions in the NFs. PCE close to 7.8% were achieved with these materials. (Table 2).

Alternatively, Archana *et al.* doped TiO<sub>2</sub> NFs with Niobium.<sup>76</sup> In this case Nb was directly incorporated in the metal oxide lattice. The primary effect was a decrease in grain size within the doped-NFs compared to the non-doped ones. It was found that the active surface area was also reduced, impacting negatively the amount of dye loaded on the doped electrodes. However, surprisingly the Jsc of DSSC with Nb-doped TiO<sub>2</sub> photoanode was found higher compared to the reference device (Table 2). This phenomenon was attributed to a higher concentration of additional charges induced by the Nb doping. Unfortunately a higher rate of recombination (originating from the smaller grain size) between the photoanode and the electrolyte was also observed leading to average performances around 4.7%. The same authors investigated Nickel doping of TiO<sub>2</sub> NFs by electrospinning Titanium (IV) isopropoxide, and Nickel sulfate hexahydrate with PVAc. After calcination, NWs

of Ni-doped TiO<sub>2</sub> showing a diameter of 60 nm and a specific surface area of *circa* 80 m<sup>2</sup>·g<sup>-1</sup> were obtained. The fibers contained up to 5% Ni atoms and this amount was sufficient to shift the band gap of the Ni doped TiO<sub>2</sub> toward the visible region.<sup>77</sup> Once incorporated in devices the fibers with 2% Ni showed high Voc (881 mV) related to its higher flat-band, and a rather high Jsc (12.01 mA·cm<sup>-2</sup>), resulting in a PCE of 6.75%. (Table 2) Ni-doped TiO<sub>2</sub> with higher content of Ni revealed lower PCE mainly because these NFs showed mixture phases of rutile and anatase in their structure.

Finally Archana *et al.* have performed the synthesis of tungsten-doped TiO<sub>2</sub> (W-TiO<sub>2</sub>) NWs by electrospinning and have evaluated their performance in DSSC.<sup>78</sup> Similarity in the ionic radii between W<sup>6+</sup> and Ti<sup>4+</sup> and availability of two free electrons per dopant were the justification for this study. Tungsten hexachloride was used as the source of W in the electrospun materials. The results showed that W-doping first hindered the grain growth leading to a larger available surface for grafting dyes, and second increased the electron lifetime on account of increased electron density. The NWs containing only 2 at.% W-TiO<sub>2</sub> gave 90% higher Jsc (15.39 mA·cm<sup>-2</sup>) compared to non-doped materials and the PCE of the best device was close to 9%.

Alternatively to elemental doping with metals, electrospun TiO<sub>2</sub> nanofibers can be coated by metals nanoparticles to provide efficient photoanodes.

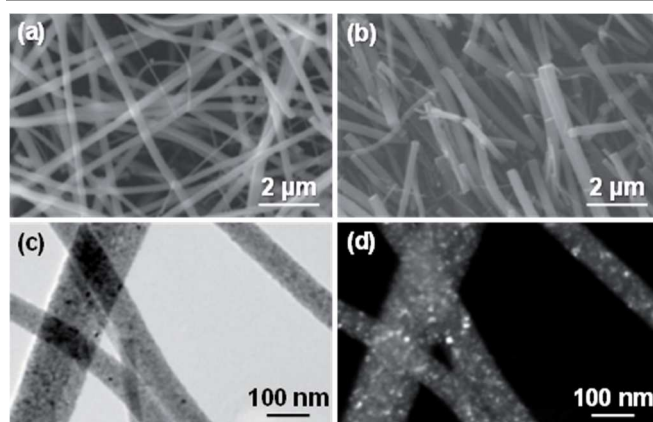


Fig. 5 a) and b) show the FE-SEM images of TiO<sub>2</sub> NFs and Au:TiO<sub>2</sub> NFs. c) shows the dark field image of Au:TiO<sub>2</sub> NFs shown in d) Reproduced with permission of ref [73]. Copyright 2014 The Royal Society of Chemistry.

This approach is quite popular in photocatalysis<sup>79</sup> but only few examples have been reported for solar cells applications. In 2011, Shi and coworkers prepared silver nanoparticle coated TiO<sub>2</sub> nanofibers by incorporating silver nitrate (AgNO<sub>3</sub>) during the electrospinning process. After the calcination step, AgNO<sub>3</sub> decomposes to form Ag nanoparticles homogeneously distributed in the fibers mat. This resulted in a significant increase of photocurrent density compared to pristine solar cells. The improvement was attributed to a better light harvesting efficiency due to the plasmon enhanced optical absorption induced by Ag nanoparticles, and to an improved electron collection efficiency resulting from faster electron transport in the Ag doped TiO<sub>2</sub> nanofiber photoanode.<sup>80</sup> More recently silver-decorated porous TiO<sub>2</sub> nanofibers were made by simple electrospinning, etching, and chemical reduction processes. The Ag NPs were well dispersed on the TiO<sub>2</sub> surface and in the photoanode film after heat treatment. The Ag NPs exhibited light scattering and plasmonic effects, thus leading to improved light absorption at visible wavelengths. Consequently, the PCE of the DSSCs was improved from 6.2% to 8.8% relative to pure TiO<sub>2</sub> NFs.<sup>81</sup> Owing to the large development of electrospun nanofibers coated by metals nanoparticles for catalysis, it appears that further improvements can be expected by implementing these materials as photoanodes in DSSCs.

### 3.1.3 Electrospun TiO<sub>2</sub> doped with carbon materials.

Over the past years carbon-based materials such as graphene and nanotubes (NTs) have emerged as valuable components for (opto)electronic applications thanks to their unique semi-conducting properties and their robustness. Several research groups have employed them to prepare blends via electrospinning process with TiO<sub>2</sub>. In 2012, Madhavan *et al.* prepared electrospun TiO<sub>2</sub>-graphene composite NFs.<sup>82</sup> The presence of graphene phase in the NFs was clearly evidenced using Raman spectroscopy and TEM. In order to maintain consistency and stability for the NFs the amount of graphene was voluntarily limited to 1 wt.%. Tests with higher contents resulted in stress and breakage of the fibers during the calcination step because of the mismatch between coefficients of thermal expansion of the two materials. One benefit of the incorporation of graphene was the reduced recombination rate of photo-induced electrons and holes in TiO<sub>2</sub> composite NFs. As a consequence a rather good PCE of 7.6% was obtained with graphene-loaded electrodes, which is higher than the PCE of 6.3% measured with pristine TiO<sub>2</sub> NFs used as reference material in this study (Table 2).

Similar observations, *i.e.* annihilation of the electron-holes recombination processes in solar cells, was reported by Motlak *et al.* for graphene oxide-doped TiO<sub>2</sub> NFs.<sup>83</sup> However the performances of the DSSC based on this material remained low (Table 2). To improve the performances the authors performed additional doping of TiO<sub>2</sub> graphene oxide photoanode with nitrogen.<sup>84</sup> The Nitrogen doping was found to produce new electronic states, narrowing the band gap and greatly improving the electron transport in TiO<sub>2</sub> NFs films thereby reducing the charge recombination rate of photon-generated electrons.

Apart from graphene derivatives, carbon nanotubes (CNT) were also employed to tune the electronic properties of electrospun materials. For example, TiO<sub>2</sub> NFs or NRs with embedded multiwall carbon nanotubes were synthesized.<sup>85,86</sup> In the case of composites with NRs of TiO<sub>2</sub>, the doping rate, ranging from 0.05 to 0.15 wt.% was simply controlled by adjusting the amount of nanotubes in the mother solution. Similarly to graphene, it was established that carbon nanotubes can significantly reduce recombination process. Besides, they can actively participate to the collection and transport of photo-generated electrons to the electrode. A very low amount of CNTs of 0.1 wt.% was found to be optimum to reach high efficiency in solar cells (Table 2), higher concentration lead to a dramatic drop of the measured J<sub>sc</sub>. This phenomenon was explained by a lower absorption of the dyes when large amounts of CNTs are used because sensitizers cannot anchor to the surface of CNTs. After optimization of the device fabrication, PCE reached 10.24% which is the highest reported for a DSSC using an electrospun photoanode (Figure 6) (Table 2).<sup>86</sup>

### 3.1.4 Alternative metal oxides for electrospun photoanode

Despite of the fact that the record efficiencies of DSSCs are obtained using nanostructures made of TiO<sub>2</sub>, other metal oxides have been successfully implemented as photo-electrodes in DSSCs<sup>87</sup> such as SnO<sub>2</sub>,<sup>88,89</sup> Nb<sub>2</sub>O<sub>5</sub>,<sup>90,91</sup> In<sub>2</sub>O<sub>3</sub>,<sup>92</sup> and ZnO.<sup>93</sup> For instance, some of these materials possess good chemical stability and they exhibit electron mobility in the bulk that is 1 to 3 orders of magnitude higher than the one of TiO<sub>2</sub>.<sup>94,95,96</sup> For this reason, some research teams have undertaken works devoted to replace TiO<sub>2</sub> by other type of metal oxide semiconductors.<sup>87</sup> Among the large variety of binary metal oxides ZnO appears to be a particularly interesting alternative material, indeed using ZnO NPs, power conversion efficiencies up to 7.5% have been reported.<sup>93,97,98</sup> ZnO is a wide-bandgap metal oxide that usually crystallizes in the hexagonal wurtzite phase. The conduction band edges of ZnO and TiO<sub>2</sub> are close (around -4.3 eV versus vacuum level) but the former shows significantly enhanced electron mobility in the bulk (200–300 cm<sup>2</sup>·V<sup>-1</sup>·s<sup>-1</sup>) than the later (0.1 cm<sup>2</sup>·V<sup>-1</sup>·s<sup>-1</sup>).<sup>99,100</sup>

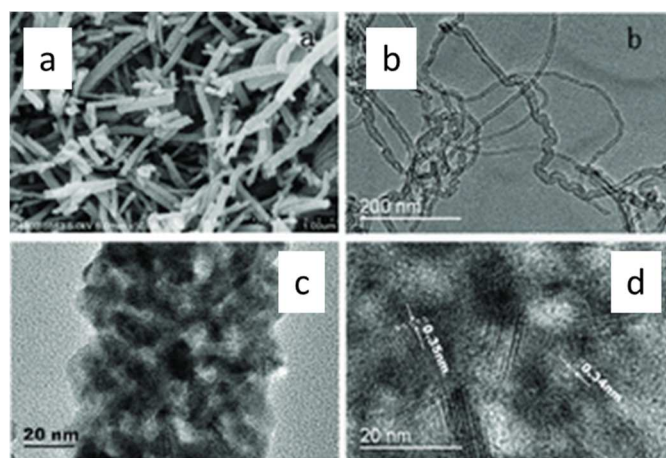


**Fig. 6** SEM and TEM images: a) SEM image of TiO<sub>2</sub> nanorods incorporating MWCNTs; b) and c) are TEM images, respectively, of MWCNTs and TiO<sub>2</sub> nanorods incorporating MWCNTs. d) HRTEM image of TiO<sub>2</sub> nanorods that incorporate MWCNTs. Reproduced with permission of ref [86]. Copyright 2013 Wiley.

**Table 2.** Photovoltaic parameters of DSSC using electrospun photoanode

<b>Doped TiO<sub>2</sub> electrospun photoanode</b>	<b>Jsc [mA·cm<sup>-2</sup>]</b>	<b>Voc [V]</b>	<b>FF [%]</b>	<b>η [%]</b>	<b>comments</b>	<b>ref</b>
TiO <sub>2</sub> NF (12 μm)	13.90	0.76	64	6.76	N3 Dye	73
TiO <sub>2</sub> NF (10 μm) + Au:TiO <sub>2</sub> NF (2 μm)	15.10	0.77	67	7.77	N3 Dye	
Reference TiO <sub>2</sub> NP (13 μm)	8.90	0.75	70	4.67	D131	76
NbTiO <sub>2</sub> NF (2 at.%) (7.8 μm)	9.74	-	-	-	D131	
Nb:TiO <sub>2</sub> NF (5 at.%) (8.2 μm)	10.00	-	-	-	D131	
Ni:TiO <sub>2</sub> NF (2 at.%) (12 μm)	12.01	0.88	64	6.75	N3	77
Ni:TiO <sub>2</sub> NF (5 at.%) (12 μm)	7.57	0.83	65	4.07	N3	
TiO <sub>2</sub> NF (12 μm)	9.68	0.81	66	5.20	N3	
Reference TiO <sub>2</sub> NP (12 μm)	12.89	0.782	70	7.09	N3	
<b>TiO<sub>2</sub>:Carbon based electrospun photoanode</b>	<b>Jsc [mA cm<sup>-2</sup>]</b>	<b>Voc [V]</b>	<b>FF [%]</b>	<b>η [%]</b>	<b>comments</b>	<b>ref</b>
TiO <sub>2</sub> /Graphene (0.7 wt.%)	16.2	0.71	66	7.6	N719	82
TiO <sub>2</sub> NF	13.9	0.71	63	6.3	N719	
TiO <sub>2</sub> /Graphene oxide (0.5 wt.%)	9.41	0.784	61	4.52	N719	83
TiO <sub>2</sub> /Graphene oxide (1.0 wt.%)	6.56	0.804	63	2.84	N719	84
TiO <sub>2</sub> NF	6.75	0.635	35	1.54	N719	
TiO <sub>2</sub> /N, Graphene oxide (0.5 wt.%)	10.82	0.815	65	5.72	N719	
TiO <sub>2</sub> /N, Graphene oxide (1.0 wt.%)	7.65	0.832	60	4.82	N719	
TiO <sub>2</sub> NF/N	11.16	0.750	56	4.70	N719	
TiO <sub>2</sub> (6.0 μm)	10.6	0.70	60.2	4.46	N719	85
TiO <sub>2</sub> /MWCNT (0.1 wt.%) (6.0 μm)	11.0	0.71	60.2	4.69	N719	
TiO <sub>2</sub> /MWCNT (0.3 wt.%) (6.0 μm)	12.0	0.79	59.4	5.63	N719	
TiO <sub>2</sub> /MWCNT (0.5 wt.%) (6.0 μm)	12.2	0.73	60.6	5.40	N719	
TiO <sub>2</sub> /MWCNT (1.0 wt.%) (6.0 μm)	11.4	0.68	49.9	3.87	N719	
Reference TiO <sub>2</sub> NP (16.7 μm)	16.30	0.74	51	6.18	N719	86
TiO <sub>2</sub> /MWCNT (0.05 wt.%) (14.5 μm)	14.20	0.76	72	7.80	N719	
TiO <sub>2</sub> /MWCNT (0.10 wt.%) (14.6 μm)	18.53	0.75	74	10.24	N719	
TiO <sub>2</sub> /MWCNT (0.15 wt.%) (13.9 μm)	12.11	0.78	76	7.13	N719	

NF: nanofibers, NP: nanoparticles, NR : nanorods, NS: nanosheet, NT: nanotubes, NW: nanowires, liquid electrolyte unless stated otherwise.

Moreover this material can also be prepared by electrospinning following pretty much the same procedures developed for TiO<sub>2</sub>. One of the first example of electrospun ZnO NFs used as photoanode was reported by Kim *et al.* in 2007.<sup>101</sup> ZnO fibers were prepared from a DMF solution containing Zn-precursor and PVAc. After hot-pressing and calcination step, fibers with grain size averaging 36 nm and showing the expected wurtzite type phase were obtained. Small surface area of the ZnO nanomaterials (around 24 m<sup>2</sup>·g<sup>-1</sup>) was the limiting factor in this work, preventing the authors to obtain high Jsc values for the solar cells and consequently a low PCE of 1.34% was reported (Table 3). In 2009, Zhang *et al.* tried to optimize this approach by preparing electrospun ZnO fibers electrodes with various thicknesses varying from 1.5 μm to 5.0 μm.<sup>102</sup> Due to the mismatch between thermal expansion coefficient of the glass substrate and ZnO, some cracks in the layer occur after

calcination steps (Fig. 7(a,b)). In order to prevent the film from such defects and to promote the adhesion of the fibers onto the FTO substrate the authors investigated the spontaneous formation of a buffer layer. They employed a Zn(OAc)<sub>2</sub> surface treatment prior to the deposition to form a dense layer that acts as a “self-relaxation layer” (Fig. 7(c)). After calcination step, the active area of the ZnO NFs was 30 m<sup>2</sup>·g<sup>-1</sup>. DSSCs were fabricated with N719 as sensitizer and the power conversion efficiency of such cells was improved to 3% (Table 3). This enhancement was explained by higher Jsc compared to previous studies, originating from a slightly larger surface area and the suppression of recombination processes between the electrode and the electrolyte as confirmed by impedance spectroscopy measurements.

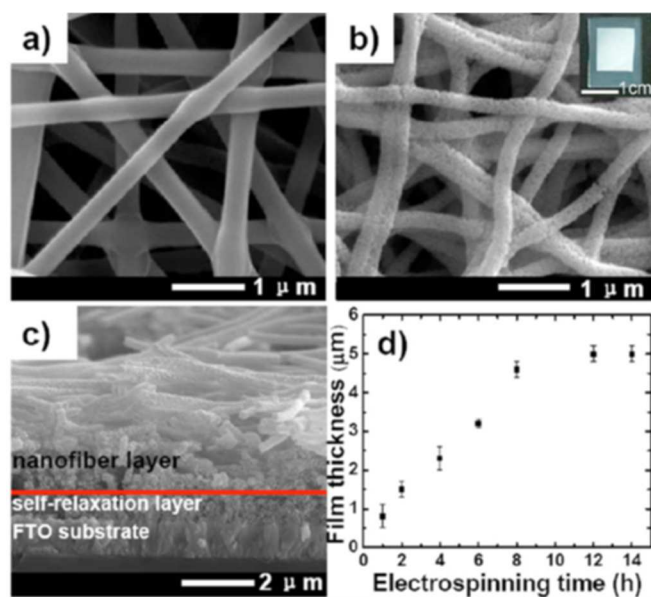


**Fig. 7** SEM images of the as-spun (a) and calcined (b) ZnO NFs on FTO substrates (inset: photograph of calcined ZnO film on FTO substrate). (c) Typical cross-sectional SEM images of the calcined ZnO film on FTO substrate. (d) The variation in ZnO film thickness with different electrospinning time. Reproduced with permission of ref [102]. Copyright 2009 The American Institute of Physics.

Later, with the objective to boost the light harvesting efficiency of ZnO NWs-based electrodes, 3D architectures were developed by McCune and co-workers.<sup>103</sup> In their work a specific electrospinning process was set up to grow a 3D multilayered ZnO NW arrays with caterpillar-like structure. Practically, the 3D structure was obtained by a layer-by-layer growth based on electrospinning. ZnO NFs are prepared on top of previously grown NWs that serve as seeding layer for the growth of the next generation of NWs. As a consequence the last layer of ZnO NWs grow upward, in a 360° fashion, along the entire length of the NFs, leading to multidimensional nanostructures (Fig. 8). After the third deposition step, the morphology changes from layer on top of each other to a caterpillar-like structure that owns extremely high density of NWs (between  $8.10^{10}$  and  $1.10^{11}$  cm<sup>-2</sup>) with small diameter (~50 nm). This unique nanostructure significantly enhances the surface area of the ZnO arrays, leading to higher short-circuit currents in solar cells. Additionally, this design resulted in closer spacing between the NWs and more direct conduction pathways for electron transfer. Thus, the open-circuit voltage was significantly improved as a direct result of the reduction in electron recombination. A PCE as high as 5.2% was achieved, which is among the highest reported values to date for ZnO nanowire-based DSSCs.

In 2015, Song *et al.* also developed ZnO electrospun photoanodes constituted by mixtures of NPs and NWs leading to PCE close to 2.6%.<sup>104</sup> They intended to improve these performances by incorporating CNTs in their NPs-NWs blends and they reached 3.8% after treating the final electrodes with TiCl<sub>4</sub>. Electrospinning was also employed to blend ZnO with TiO<sub>2</sub> and graphene following the procedure initially developed

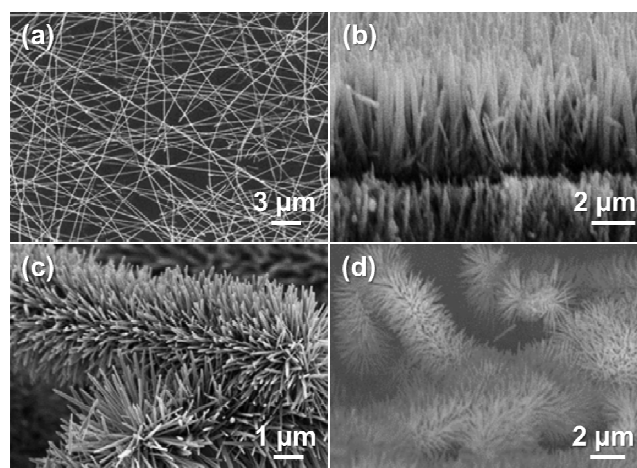


**Fig. 8** SEM images: (a) ZnO NFs electrospun on FTO substrate; (b) two distinct layers of ZnO nanowire array; (c) close-up view of highly dense "caterpillar-like" ZnO nanowire structures; (d) multiple layers (3–5) of ZnO nanowire array illustrating the distinct layers of the "caterpillar-like" ZnO nanowire structures. Reproduced with permission from ref [103]. Copyright 2012 American Chemical Society.

by Madhavan *et al.*<sup>82,105</sup> Mixing ZnO with TiO<sub>2</sub> was motivated by the fact that the conduction band of TiO<sub>2</sub> is located at -4.2 eV whereas the one of ZnO is slightly lower in energy -4.3 eV. This difference can be beneficial to increase the lifetime of the electrons by promoting electron transfer from the TiO<sub>2</sub> conduction band to the one of the ZnO. Graphene was investigated in this work as a separation layer. Its role was to favour the separation of the photo-induced excitons and to prevent their recombination thanks to the band bending that occurs at the interface with the ZnO-TiO<sub>2</sub> blend. The use of ZnO-TiO<sub>2</sub> blend as photoanode yielded a PCE of 2.7 % whereas employing the graphene doped blend the PCE reached 3.7 % (Table 1). Co-axial electrospinning techniques initially developed for the formation of TiO<sub>2</sub> hollow structure, were implemented by Du *et al.* to form NFs consisting in a TiO<sub>2</sub> core surrounded by a ZnO sheath.<sup>106</sup> This strategy was successful and led to the effective suppression of some recombination processes that yielded PCE of 5.2%.

Apart from ZnO, Tin oxide (SnO<sub>2</sub>) is also identified as a useful transparent conducting oxide for nanoelectronics due to its high electron mobility in bulk (10-125 cm<sup>2</sup>·V<sup>-1</sup>·s<sup>-1</sup>) and its wider band gap (circa 3.6 eV). Krishnamoorthy *et al.* extended the technique they developed to form vertically aligned TiO<sub>2</sub> NFs to SnO<sub>2</sub>.<sup>71,107</sup> They demonstrated a large-scale production of aligned SnO<sub>2</sub> NFs with a multi-nozzle electrospinning method combined with an air-shield enclosed rotating drum collector. The height and diameter of the NWs were  $19 \pm 2$  μm and  $75 \pm 25$  nm respectively and XRD patterns revealed that the SnO<sub>2</sub> NWs are polycrystalline rutile structures. DSSCs using this nanostructured material as photoanode gave a short-circuit J<sub>sc</sub> of 9.9 mA·cm<sup>-2</sup>, a Voc of 0.525 V and a PCE of 2.53 % (Table 3). These results were comparable to DSSCs consisting of randomly aligned NWs produced by hydrothermal synthesis, or thick mesoporous SnO<sub>2</sub> NPs.<sup>108</sup> The rather low Voc usually observed for DSSCs fabricated with a SnO<sub>2</sub> photoanode (typically below

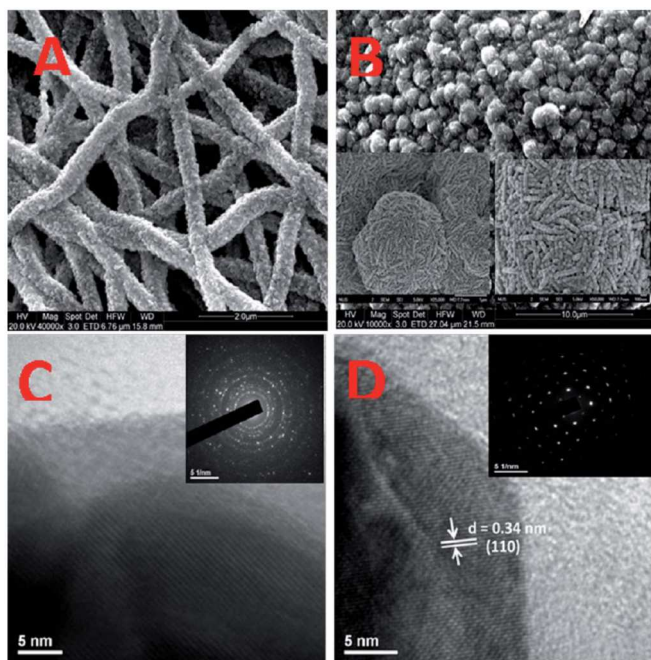


**Fig. 9** SEM images (A & B) and HRTEM images (C & D) of fibers and flowers, respectively. Insets: (B) magnified SEM images of the flower morphology; (C) selected area electron diffraction (SAED) pattern showing polycrystalline rings; and (D) SAED pattern of flowers showing single crystalline spotty patterns. Reproduced with permission from ref [109]. Copyright 2012 The Royal Society of Chemistry.

600 mV) is due to the position of its conduction band which is located at a lower energy level compared with  $\text{TiO}_2$ . Kumar *et al.* explored further the versatility of electrospinning by precisely controlling the precursor concentration (anhydrous tin (II) chloride) in the polymeric solution (DMF-Ethanol-PVAc) to obtain either fibers or flower shaped nanostructures of  $\text{SnO}_2$ .<sup>109</sup> The nanoflowers were made of nanofibrils with diameters ranging from 70 to 100 nm, which in turn consisted of linear arrays of single crystalline NPs of 20 to 30 nm size (Fig. 9). XPS and XRD analysis of the nanostructures showed that both nanoflowers and NFs have the same chemical composition and show the same cassiterite phase, however the nanoflowers revealed a superior crystallinity. DSSCs were fabricated using the different materials, highlighting the better performances of the nanoflowers-based device which PCE reached 3% (Table 3). Surprisingly the  $V_{oc}$  of the solar cells was impressively high for a  $\text{SnO}_2$ -based device at 0.7 V. This was tentatively explained by a faster charge collection in the nanoflower structures due to their superior crystallinity, allowing to suppress significantly the surface defects and interfacial recombination processes between the semiconductor and the electrolyte.

In order to solve the  $V_{oc}$  issue usually observed with  $\text{SnO}_2$  photoanodes while keeping their transport ability, Gao *et al.* developed  $\text{SnO}_2$  nanotubes and  $\text{SnO}_2$ - $\text{TiO}_2$  core-shell NFs.<sup>110</sup> Nanotubes were obtained starting from precursor solutions with lower concentration compared to the ones that usually lead to NFs. It was hypothesized that upon heating, the diluted  $\text{SnCl}_2$  precursors dispersed in the PVP solution tend to diffuse to the surface of the NFs and to decompose to form  $\text{SnO}_2$  NPs whereas

using the more concentrated solutions, fibers are formed after decomposing the precursors without any migration. This formation mechanism of  $\text{SnO}_2$  hollow structures was also investigated by other teams who proposed complementary interpretations.<sup>111,112</sup> Coating of  $\text{TiO}_2$  on  $\text{SnO}_2$  NFs and nanotubes electrodes was performed by dipping the  $\text{SnO}_2$  NFs and nanotubes electrodes into a  $\text{TiCl}_4$  aqueous solution followed by sintering. XRD analysis showed that both  $\text{SnO}_2$  and  $\text{TiO}_2$  were in a rutile phase. The surface area was increased from circa  $39 \text{ m}^2 \cdot \text{g}^{-1}$  to  $52 \text{ m}^2 \cdot \text{g}^{-1}$  after coating with  $\text{TiO}_2$  the  $\text{SnO}_2$  nanotubes.

The devices using the bare and coated NFs and nanotubes show that the  $V_{oc}$  and  $J_{sc}$  of the coated photoanode are considerably higher than those obtained with the bare ones (Table 3). These results were expected because the conduction-band edge of  $\text{SnO}_2$  is 300 mV more positive than that of  $\text{TiO}_2$ , which leads to a faster interfacial electron recombination and lower trapping density. Therefore, the significant increases in  $V_{oc}$  and  $J_{sc}$  indicate that the interfacial electron combinations in  $\text{SnO}_2$  NFs and nanotubes photoanode are effectively suppressed by coating them with  $\text{TiO}_2$ . Gao *et al.* recently developed a new procedure to tune the architecture of the  $\text{SnO}_2$ - $\text{TiO}_2$  NFs.<sup>113</sup> They managed to grow  $\text{TiO}_2$  needles at the surface of the NFs from a  $\text{TiCl}_3$  solution heated at  $75^\circ\text{C}$ . High  $J_{sc}$  ( $20.5 \text{ mA} \cdot \text{cm}^{-2}$ ) was achieved with this new architecture, that was attributed to a lower charge recombination and a faster electron transport.

In 2013 Ahn *et al.* used a similar approach to cover the  $\text{SnO}_2$  nanotubes with  $\text{TiO}_2$  nanosheets grown via hydrothermal reaction (Fig. 10).<sup>110,114</sup> These nanotubes were dispersed in mesoporous  $\text{TiO}_2$  films. The coated nanotubes exhibit a superior light harvesting efficiency originating from a better light scattering ability.

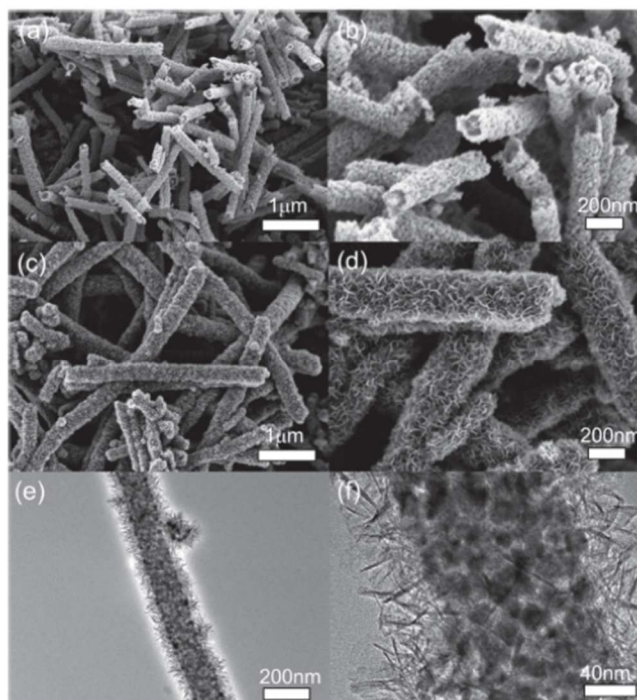


**Fig. 10** a, b) Field emission scanning electron microscopy (FE-SEM) images of pristine  $\text{SnO}_2$  nanotubes c, d) FE-SEM images of  $\text{SnO}_2$  nanotube@ $\text{TiO}_2$  nanosheet. e, f) TEM images of  $\text{SnO}_2$  nanotube@ $\text{TiO}_2$  nanosheet. Reproduced with permission of ref [114]. Copyright 2013 Wiley.

These photoanodes also show a bimodal porosity consisting of small and big pores that enable good penetration of electrolyte making them suitable for quasi-solid state DSSC.  $\text{SnO}_2$ - $\text{TiO}_2$  coated nanotubes showed better efficiency, reaching 7.7% with electrodes containing 10 wt.% of coated nanotubes.

In 2010 Wu *et al.* developed a scattering layer of  $\text{SnO}_2$  and ZnO on top of ZnO NWs-based photoanode.<sup>115</sup> The electrospun PVP-hosted  $\text{SnO}_2$ /ZnO NFs were swollen using methanol vapor followed by high-temperature calcination at 600 °C to form a layer composed of  $\text{SnO}_2$  and ZnO nanocrystals with a diameter of ~10 nm. The NFs of ZnO and  $\text{SnO}_2$  were also obtained without vapor treatment.  $J_{sc}$ ,  $V_{oc}$ , and FF of the devices fabricated with this type of scattering layers are enhanced compared to pristine ones. IPCE spectra and IMPS results show that the dye-sensitized  $\text{SnO}_2$ -ZnO films does not contribute directly to the generation of photocurrent, the enhancement of  $J_{sc}$  can mainly be attributed to the reflection of photons back into the nanowire photoanode. Lately some teams have reported the use of electrospun  $\text{In}_2\text{O}_3$  as photoanode for DSSCs but their efficiency was limited below 0.5%.<sup>116,117</sup> To improve these results, in 2015, Miao *et al.* attempted to use electrospinning methods for the synthesis of indium oxide nanotubes doped with rare earth element such Dysprosium, Holmium and Erbium.<sup>118</sup> The structure analysis of these new photoanodes confirmed that the different rare earth elements were incorporated into the cubic crystal lattice of  $\text{In}_2\text{O}_3$ . The band gap of the doped indium oxide photoanode was slightly larger due to charge transfer transition between these ions and indium oxide conduction band and also to the formation of localized band edges at the doped sites in the  $\text{In}_2\text{O}_3$  lattice. DSSC based on these doped photoanodes show better performances than the undoped ones. Doping with Erbium gave the best result with a PCE of 1.4% compared to 0.5% obtained with undoped  $\text{In}_2\text{O}_3$  (Table 3).

Besides the simple binary metal oxides, ternary metal oxides have also been considered as photoelectrode materials in DSSC. In contrast, electrospinning of multication oxides has been rarely explored. In comparison with simple binary oxides, multication oxides show more possibilities to tune the materials' chemical and physical properties by altering the compositions. By varying the relative element ratio, the band gap energy, the work function, and the electric resistivity of the ternary oxides can be readily tuned. Considering the availability of a wide range of multication oxides and their tuneable properties, it is therefore interesting to investigate their applications in DSSC and for their preparation electrospinning appears as a particularly well-adapted method. Up to now, electrospun ternary oxides such as  $\text{SrTiO}_3$  fibers<sup>119,120,121</sup> have been principally investigated for photo-catalysis and only few articles are focused on electrospun  $\text{Zn}_2\text{SnO}_4$  nanomaterials for photovoltaic applications.<sup>122,123,124,125</sup> The main motivation in developing nanostructures made of  $\text{Zn}_2\text{SnO}_4$  rely on its lower sensitivity to acidic conditions compared to ZnO and its higher electron mobility in bulk compared to  $\text{TiO}_2$ . In 2013, Choi *et al.* prepared electrospun  $\text{Zn}_2\text{SnO}_4$  photoanode that were sensitized with N719 and also organic dyes.<sup>126</sup> The  $\text{Zn}_2\text{SnO}_4$  photoanodes were prepared by electrospinning of a mother solution made of  $\text{Zn}(\text{OAc})_2$ ,  $\text{Sn}(\text{OAc})_4$  and PVAc, followed by a hot-pressing step to ensure

adhesion to the FTO surface that partially melts the PVAc onto the FTO before a calcination step. Calcination at 450 °C gives porous and smooth amorphous NFs as confirmed by TEM and X-ray diffraction patterns (Fig. 11). The specific surface area for this NFs network was found to be 124  $\text{m}^2\cdot\text{g}^{-1}$ , which is similar to conventional  $\text{TiO}_2$  NPs electrode. Results obtained using organic and organometallic sensitizers clearly showed that  $\text{Zn}_2\text{SnO}_4$  photoanodes give better performances when they are combined with organic sensitizers. Power conversion efficiency with organic dyes leads to PCE up to 3.7% whereas the PCE with N719 was limited to 1.4% for similar photoanode thickness (3  $\mu\text{m}$ ) (Table 3). The better efficiency with organic dyes was originating from much higher  $J_{sc}$  attributed to a better dye loading and their higher extinction molar coefficient compared to N719. This work paved the way for further improvements. Indeed, recently, hierarchically structured  $\text{Zn}_2\text{SnO}_4$  beads synthesised by hydrothermal method and deposited by electro-spray technique have demonstrated PCE of 6.3%.<sup>127</sup>

### 3.2 Electrospun materials as electrolyte in DSSC

We have seen previously that electrospun NFs and mats are nowadays increasingly being investigated for the development of photoanode materials, where nanoscale features such as high

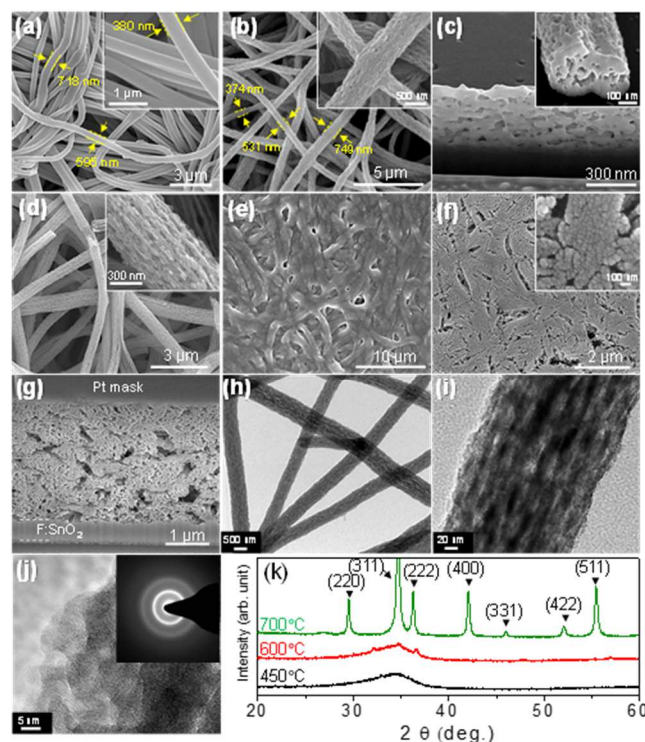


**Fig. 11** a) SEM image of as-spun  $\text{Zn}(\text{OAc})_2$ - $\text{Sn}(\text{OAc})_4$ /PVAc composite fibers; b) SEM image of  $\text{Zn}_2\text{SnO}_4$  fibers calcined at 500°C; c) cross-sectional view of  $\text{Zn}_2\text{SnO}_4$  fibers calcined at 500°C; d)  $\text{Zn}_2\text{SnO}_4$  fibers calcined at 700 °C (reference); e) hot-pressed  $\text{Zn}(\text{OAc})_2$ - $\text{Sn}(\text{OAc})_4$ /PVAc composite fibers; f) SEM image of  $\text{Zn}_2\text{SnO}_4$  fibers calcined at 450 °C after hot-pressing step; g) cross-sectional view of  $\text{Zn}_2\text{SnO}_4$  fibers calcined at 450 °C after hot-pressing step; h) TEM image of  $\text{Zn}_2\text{SnO}_4$  fibers calcined at 450 °C after hot-pressing step; i) magnified TEM image in (h); j) magnified TEM image of (i) and the inset shows the SAED pattern; k) X-ray diffraction pattern of  $\text{Zn}_2\text{SnO}_4$  fibers calcined at various temperatures of 450 °C, 600 °C, and 700 °C. Reproduced with permission of ref [126]. Copyright 2013 Wiley.

aspect ratios and large surface area combined to high pore volume allow improvements of the performances of solar cells. However electrospinning is such a powerful technique that it can also be applied for the processing of other key elements in DSSCs such as electrolyte and counter electrode. For real use of DSSCs and future applications in BIPV for instance, in addition to high PCEs, long device lifetimes are required. Because of this requirement, highly volatile electrolytes, such as acetonitrile-based ones, have to be replaced because they are inappropriate for achieving high stability.

One of the clearly identified problems employing them is the difficulty to find robust sealing, and their tendency to evaporation and leakage. Many research groups have been searching for alternatives to liquid electrolytes, such as inorganic or organic hole conductors, ionic liquid, and gel electrolytes. In particular, polymer gel electrolytes have attracted interest due to their appealing properties such as thermal stability, non-flammability, small vapour pressure, good pore filling properties and high ionic conductivity, which is achieved by trapping a liquid electrolyte in polymer cages formed in a host matrix. A wide variety of polymers have already been employed and studied over the years such as poly(acrylonitrile),<sup>128</sup> poly(ethyleneglycol),<sup>129</sup> poly(methylmethacrylate) (PMMA),<sup>130</sup> and poly(VinylideneFluoride-co-HexaFluoroPropylene) (PVdF-HFP)<sup>131</sup> to name a few. So far PVdF-HFP looks to be the most promising system due to its high ionic conductivities at room temperature and its stability and compatibility with TiO<sub>2</sub> photoanode and Pt counter electrode.

In 2008, Priya *et al.* investigated a method to process polymer gel electrolytes via electrospinning to generate a fibrous membrane of PVdF-HFP.<sup>132</sup> The membrane was prepared from a 16 wt.% solution of PVdF-HFP in a mixture of acetone/N,N-dimethylacetamide at 80 °C. The resulting membrane thickness was reduced from 30 to 15 μm after a drying step followed by a hot-pressing step. The average length of the NFs was estimated to be 600 nm while the ionic conductivity of the membrane was measured at *circa* 1.10<sup>-5</sup> S·cm<sup>-1</sup> at 25 °C (Table 4). To fabricate the DSSC, the membrane was simply sandwiched between the sensitized photoanode (sensitizer N719) and the counter electrode and the cell was filled with iodine electrolyte before being thermally sealed. Photovoltaic measurements showed that the final device exhibits higher Voc but lower Jsc than the reference device containing solely a liquid electrolyte. The reduction in the back electron transfer from the TiO<sub>2</sub> CB to the I<sub>3</sub><sup>-</sup> ions because of a lower concentration of I<sub>3</sub><sup>-</sup> species in the electrolyte near the mesoporous TiO<sub>2</sub> was hypothesised to explain the enhancement of Voc value. Unfortunately this phenomenon is also detrimental to the Jsc, and because of lower ionic conductivity, the dye regeneration kinetic is not as fast as in liquid cells. The photoconversion efficiency was lower compared to the liquid device but the cells demonstrated higher fatigue resistance. Indeed the PVdF-HFP based device retained 96% of their efficiency after two weeks (compared to 85% for reference devices). Later Ahn *et al.* further enhanced the performances of PVdF-HFP-based devices by developing a new system composed of liquid crystal embedded polymer electrolytes.<sup>133</sup> The role of the liquid crystal was to act as

plasticizer. As a result ionic conductivity was enhanced in the presence of this additive and reached values close to the ones observed with standard liquid electrolyte (Table 4). The quasi solid-state DSSC fabricated from electrospun fibers comprising the additive reached a maximum PCE of 6.82%. With the same philosophy, *i.e.* boosting the ionic conductivity by means of additives, Vijayakumar *et al.* have developed PVdF-HFP layers with various amounts of cobalt sulphide (CoS) using electrospinning technique.<sup>134</sup> Nanocomposite membranes were activated by an ionic liquid electrolyte. Authors found that, even with limited amount (up to 3 wt.%) of CoS NPs uniformly dispersed in the matrix, the charge transport was increased and that the diffusion of the redox couple in the electrolyte system was facilitated. The photovoltaic performance of the DSSCs assembled using this new material was found to be 7.34%. It is worth noting that the incorporation of the CoS NPs is not detrimental for the stability of the cells. The same team also studied the swelling of PVdF-HFP electrospun fibers using ionic liquid electrolyte giving a power conversion efficiency of 6.42% and an excellent stability over more than 30 days.<sup>135</sup> Following the same approach polyaniline (PANI) was mixed into the PVdF-HFP membrane.<sup>136</sup> PANI facilitates electrical conduction and ultimately accelerates redox reaction kinetics. As a result power conversion efficiency was improved from 6.42% for pristine layers to 7.20% with 3 wt.% of PANI in the PVdF-HFP matrix. Lately, Sethupathy *et al.* electrospun another type of blend based on poly(vinylidene fluoride-co-polyacrylonitrile) (PVdF-PAN) and Fe<sub>2</sub>O<sub>3</sub> NPs.<sup>137</sup> Similarly to CoS in composites with PVdF-HFP, Fe<sub>2</sub>O<sub>3</sub> NPs increased ionic conductivity in the deposited layer, but the PCE of the devices was limited to 4.90% in this case (Table 4).

### 3.3 Electrospun materials as counter electrodes in DSSC

Platinum counter electrodes have been widely used in DSSCs, because Platinum is an efficient electro-catalyst for reduction of I<sub>3</sub><sup>-</sup> ions.<sup>138</sup> Nowadays, Platinum still appears as a reference system in the field but this metal is also known for being an expensive element that prevents further massive developments at the industrial level. Besides, side reactions (such as oxidation and complex formation) with the corrosive I<sup>-</sup>/I<sub>3</sub><sup>-</sup> redox couple can reduce its catalytic activity, which can jeopardize the long-term stability of DSSCs.<sup>139,140</sup> For the above mentioned reasons it comes out highly desirable to replace this component in DSSCs or to significantly diminish the quantity of Pt necessary to fabricate them. The first example of electrospun Pt-free counter-electrode was published in 2010.<sup>141</sup> In this work Platinum was replaced by carbon NFs synthesized according to the following process: in a first step, NFs were simply prepared from a DMF-Poly(acrylonitrile) solution that was electrospun using standard conditions, then the fibers were collected and subsequently heated at 1200 °C to give rise to the formation of carbon nanofibers (CNFs). Those fibers were then dispersed into poly(oxyethylene-tridecylether) and printed using a doctor-blade onto a FTO glass substrate. Processing the NFs by blending them with a polymer matrix appeared mandatory since they could not provide alone enough strong attachment to the FTO surface.

**Table 3.** Alternative semiconducting oxide for electrospun photoanode

Photoanode	Jsc [mA.cm <sup>-2</sup> ]	Voc [V]	FF [%]	η [%]	Comments	ref
ZnO NF (1,5 μm)	3.58	0.6	62	1.34	N719	101
ZnO NF (1,5 μm)	4.58	0.63	61	1.77	N719	102
ZnO NF (3,2 μm)	6.10	0.61	64	2.36	N719	
ZnO NF (5,0 μm)	6.62	0.59	66	2.58	N719	
ZnO NF (5,0 μm, Zn(Oac) <sub>2</sub> treatment)	9.14	0.57	58	3.02	N719	
ZnO 2 layers (50 mM precursor solution)	4.45	0.51	40	0.91	N719	103
ZnO 5 layers (50 mM precursor solution)	10.16	0.56	43	2.45	N719	
ZnO 2 layers (75 mM precursor solution)	8.69	0.67	59	3.43	N719	
ZnO 5 layers (75 mM precursor solution)	15.20	0.69	50	5.20	N719	
ZnO NP	5.2	0.621	46.5	1.5	N719	104
ZnO NP: ZnO NW (20 wt.%)	6.29	0.672	61.5	2.6	N719	
ZnO NW	5.41	0.653	45.3	1.6	N719	
(ZnO NP:MWCNT): (ZnO NW: MWCNT) (20 wt.%)	7.27	0.693	59.5	3	N719	
ZnO NP: ZnO NW (20 wt.%) TiCl <sub>4</sub> treatment	7.59	0.7	60.2	3.2	N719	
(ZnO NP:MWCNT): (ZnO NW: MWCNT) (20 wt.%) TiCl <sub>4</sub> treatment	8.48	0.732	61.2	3.8	N719	
TiO <sub>2</sub> :ZnO	6.3	0.73	57	2.70	N719	105
TiO <sub>2</sub> :ZnO:Graphene (0.7 wt.%)	9.4	0.71	56	3.70	N719	
TiO <sub>2</sub> :ZnO NF (core sheath)	11.3	0.75	61	5.17	N719	106
TiO <sub>2</sub> NF	10.6	0.70	60	4.47	N719	
SnO <sub>2</sub> NP (3 μm)	2.38	0.52	41	0.50	N719	107
SnO <sub>2</sub> NP (3 μm) + SnO <sub>2</sub> NW (19 μm)	9.90	0.53	49	2.53	N719	
SnO <sub>2</sub> nanoflowers (15 μm)	7.30	0.7	60	3.00	N3	109
SnO <sub>2</sub> NF(15 μm)	3.00	0.6	38	0.71	N3	
SnO <sub>2</sub> NF	4.51	0.50	31	0.71	N719	110
SnO <sub>2</sub> NT	5.89	0.49	35	0.99	N719	
Core shell SnO <sub>2</sub> NF-TiO <sub>2</sub>	12.69	0.74	49	4.61	N719	
Core shell SnO <sub>2</sub> NT-TiO <sub>2</sub>	14.71	0.72	48	5.11	N719	
Reference TiO <sub>2</sub> NP	11.44	0.73	58	4.82	N719	
SnO <sub>2</sub> NF	7.04	0.51	38	1.34	N719	113
Core shell SnO <sub>2</sub> NF-TiO <sub>2</sub>	9.80	0.59	37	2.11	N719	
Core shell SnO <sub>2</sub> NF-needle TiO <sub>2</sub>	20.5	0.71	48	7.06	N719	
Reference NP	11.7	0.75	58	5.04	N719	
Organized mesostructured (OM) TiO <sub>2</sub> NP (8.5 μm)	13.1	0.76	60	6.0	N719, solid state (PEBII)	114
OM TiO <sub>2</sub> /SnO <sub>2</sub> NT (7 wt%) (8.5 μm)	14.5	0.73	54	5.7	N719, solid state (PEBII)	
OM TiO <sub>2</sub> / SnO <sub>2</sub> NT (10 wt%) (8.5 μm)	13.9	0.70	49	4.9	N719, solid state (PEBII)	
OM TiO <sub>2</sub> /SnO <sub>2</sub> NT @ TiO <sub>2</sub> NS (7 wt%) (8.5 μm)	16.2	0.75	57	6.9	N719, solid state (PEBII)	
OM TiO <sub>2</sub> /SnO <sub>2</sub> NT @ TiO <sub>2</sub> NS (10 wt%) (8.5 μm)	17.4	0.77	58	7.7	N719, solid state (PEBII)	
ZnO NW (3 μm) + SnO <sub>2</sub> /ZnO NF scattering layer	2.66	0.54	51	0.74	D149	115
ZnO NW (3 μm) + SnO <sub>2</sub> /ZnO nanofilm scattering layer	2.99	0.57	59	1.01	D149	

ZnO NW (3 μm)	2.46	0.44	53	0.58	D149	
In <sub>2</sub> O <sub>3</sub>	4.6	0.4	26.2	0.5	N719	118
In <sub>2</sub> O <sub>3</sub> :Dy <sup>3+</sup>	6.6	0.5	33.4	1.1	N719	
In <sub>2</sub> O <sub>3</sub> :Ho <sup>3+</sup>	6.7	0.5	33.2	1.1	N719	
Zn <sub>2</sub> SnO <sub>4</sub> NF (1.5μm)	6.39	0.73	59	2.77	TA-TV-CA	126
Zn <sub>2</sub> SnO <sub>4</sub> NF (3μm)	8.11	0.72	63	3.67	TA-TV-CA	
Zn <sub>2</sub> SnO <sub>4</sub> NF (4μm)	7.66	0.75	62	3.55	TA-TV-CA	
Zn <sub>2</sub> SnO <sub>4</sub> NF (4μm)	2.75	0.74	69	1.40	N719	

NF: nanofibers, NP: nanoparticles, NR : nanorods, NS: nanosheet, NT: nanotubes, NW: nanowires, liquid electrolyte unless stated otherwise.

**Table 4.** Photovoltaic performances of electrospun polymer gel electrolyte-based device

Polymer gel Electrolyte	Jsc [mA.cm <sup>-2</sup> ]	Voc [V]	FF [%]	η [%]	ionic conductivity [S.cm <sup>-1</sup> ]	ref
PVdF-HFP <sup>a</sup>	15.57	0.76	62	7.3	~1 10 <sup>-5</sup>	132
liquid <sup>a</sup>	16.86	0.73	63	7.8	-	
PVdF-HFP <sup>b</sup>	13.65	0.7	67	6.35	2.1 10 <sup>-3</sup>	133
E7 + PVdF-HFP <sup>b</sup>	14.62	0.72	65	6.82	2.9 10 <sup>-3</sup>	
liquid <sup>b</sup>	14.71	0.75	65	7.17	3.2 10 <sup>-3</sup>	
PVdF-HFP <sup>c</sup>	13.10	0.71	69	6.42	5.83 10 <sup>-3</sup>	134
CoS 1 wt% + PVdF-HFP <sup>c</sup>	14.42	0.73	70	7.34	36.43 10 <sup>-3</sup>	
PANI 3 wt% + PVdF-HFP <sup>c</sup>	14.30	0.72	70	7.20	31.44 10 <sup>-3</sup>	135
Fe <sub>2</sub> O <sub>3</sub> 3 wt% + PVdF-PAN <sup>a</sup>	9.6	0.75	55	3.96	6.30 10 <sup>-2</sup>	137
Fe <sub>2</sub> O <sub>3</sub> 5 wt% + PVdF-PAN <sup>a</sup>	10.0	0.76	56	4.30	6.42 10 <sup>-2</sup>	
Fe <sub>2</sub> O <sub>3</sub> 7 wt% + PVdF-PAN <sup>a</sup>	10.4	0.77	62	4.90	6.81 10 <sup>-2</sup>	

<sup>a</sup> Electrolyte composition: 0.6 M 1-hexyl-2,3-dimethylimidazolium iodide, 0.1 M LiI, 0.05 M I<sub>2</sub>, and 0.5 M 4-tert-butylpyridine in ethylene carbonate/ propylene carbonate (1:1 wt.%), dye: N719; <sup>b</sup> Electrolyte composition: iodine, tetrabutylammonium iodide, 1-propyl-3-methylimidazolium iodide (PMII) as an ionic liquid, ethylene carbonate /propylene carbonate (3/1 as weight ratio), dye: N719; <sup>c</sup> Electrolyte composition: 0.5 M LiI, 0.05 M I<sub>2</sub>, 0.5 M 4-tert-butylpyridine and 0.5 M 1-butyl-3-methylimidazolium iodide, dye N719.

When processed into a paste, the NFs, which were originally tens of micrometers long, were broken into sub-micrometers to micrometers. That impacted the conductivity which was one order of magnitude lower (1538 S.m<sup>-1</sup> to 164 S.m<sup>-1</sup>). Photovoltaic performances of the Pt-free electrodes (PCE of 5.5%) were slightly lower than the reference Pt-based counter-electrode, mainly originating from an increase of the total series resistance of the device. With the goal to maintain efficiency for the regeneration process of the redox species and to significantly reduce the quantity of Pt used in the counter electrodes, Pt NPs were incorporated in electrospun carbon fibers (CNFs). In this study, the CNF were prepared by electrospinning polyacrylonitrile nanofibers followed by thermal treatments of stabilization and carbonization. Then, crushed CNFs were soaked into a Pt precursor solution and heated at 400°C. The CNF-Pt composite were then mixed with carboxymethyl cellulose (CMC) and sodium salt in deionized water was added as a binder to give a printable paste. That paste was applied onto the FTO coated glass substrate by doctor blading. Using this material, the total resistance of the DSSC decreases and the devices with a CNF-Pt-based counter electrode exhibit a PCE of 8%.<sup>142</sup> These authors also developed electrospun nano-belt consisting of overlaid TiC/C composite NFs where the surface was decorated with Pt NPs.<sup>143</sup> This approach led to Pt counter-

electrodes where the quantity of Pt was 10 times inferior compared to conventional devices. Their catalytic activity was good enough to reach PCE of *circa* 7.2%, but this was not sufficient to outperform above-mentioned performances. More recently, Elbohy *et al.* integrated graphene nano-platelets into electrospun CNFs and they subsequently grown Pt nano-needles onto the CNFs surface through a redox reaction between H<sub>2</sub>PtCl<sub>6</sub> and HCOOH.<sup>144</sup> Synergistic effects of graphene integration and Pt nano-needle decoration on DSC performance were observed. They were attributed to higher electro-catalytic performance due to larger interfacial area, faster I<sup>3-</sup> reduction rate, lower charge transfer resistance, and lower series resistance for electron transport. Overall this yielded to PCE of 9.77%. (Table 5)

In order to get rid of Platinum, Nickel is a plausible alternative. However to reach respectable efficiency it has to be either nitride,<sup>145</sup> embedded in graphene as nickel phosphide<sup>146</sup> or processed as nanoparticle.<sup>147</sup> Joshi *et al.* followed that last strategy and produced a counter electrode from Nickel NPs embedded in carbon nanotubes and NFs.<sup>148</sup> To form the nickel-embedded CNT-coated electrospun NFs, Poly(acrylonitrile) and Ni(AcAc)<sub>2</sub> were dissolved in DMF and then the precursors solution was electrospun. The NFs were then annealed in a mixed H<sub>2</sub> and Argon flow to reduce Ni<sup>2+</sup> to Ni atom. This forces the aggregation of Ni at the NFs surface to form catalytic NPs.

Following that step, NFs were fully carbonized before growing nanotubes by introducing a flow of Argon and ethylene. The resulting materials are then crushed, mixed with carboxymethyl cellulose sodium salt to give a paste that can be deposited by doctor blading onto a FTO glass substrate to give the counter electrode. The new counter electrode was roughly half the thickness of the reference electrode but it revealed greater porosity and surface area and therefore better catalytic activity. Despite of being lower, the DSSC performances with Ni-based electrodes were very close to the ones of Pt-based devices (7.96% versus 8.32%) (Table 5). In 2015, Saranya *et al.* swap from Ni NPs to a bimetallic Fe-Ni system and followed the electrospinning procedure.<sup>149</sup> They were able to attain the equivalent electrochemical parameters to Pt-based counter-electrode with this new material and reported very close photovoltaic efficiencies (Table 5). Mohamed *et al.* selected (Co-Cr) NPs to be embedded into CNFs to boost their electrocatalytic activity.<sup>150</sup> However, their approach was not fully successful as the performances were lower. Therefore they replaced Cr in their material by Ni and they achieved slightly better performances close to 4.5% (Table 5).<sup>151</sup>

Conducting polymers were also considered for developing original Pt-free counter electrodes materials. In 2012, Peng *et al.* used electrospun conductive polyaniline-poly(lactic acid) (PLA) composite NFs for the fabrication of rigid and flexible devices.<sup>152</sup> PLA was necessary to increase the viscosity and surface tension of the solution to form NFs during electrospinning, and PANI was doped with camphor sulfonic acid (CSA) to make it more conductive. One strong advantage of this approach is the absence of annealing process to form the electrode. The as-spun PANI-CSA-PLA NFs are stacked and bonded with the substrate firmly, immediately after deposition resulting in an interconnected nanofibrous network (Fig. 12). A quite promising PCE of 5.3% was obtained for the devices containing PANI-CSA-PLA counter-electrode. Because annealing step is not necessary with this kind of materials, the process is fully compatible with flexible substrate, and the authors demonstrated its applicability on polyethylene naphthalate (PEN) (Table 5).

In 2013 Kim *et al.* developed platinum NFs in order to get rid of the FTO that is used in the counter electrode.<sup>153</sup> The electrospinning process allowed the authors to prepare Pt NFs from a PVP solution containing the Pt source ( $\text{H}_2\text{PtCl}_6 \cdot 6 \text{H}_2\text{O}$ ) and thermal annealing was employed to decompose the PVP and reduce the precursor to give pure metallic Pt. By controlling the electrospinning time it is possible to control the NFs density on the bare glass substrate onto which they are deposited. The NFs density clearly impacts the sheet conductance and the charge transfer resistance. The benefits of this approach were limited as, Pt is still used to fabricate the electrodes and the PCE remains moderate (Table 5). In 2015, Zhou *et al.* reported a similar approach to form Pt NWs mats as counter electrode that were used in flexible cells.<sup>154</sup> Even if the electrocatalytic behaviour of those Pt counter electrode was found to be similar to conventional Pt/FTO counter electrode the photovoltaic performances were relatively poor (3.82%). Kesterite is another class of material that was recently investigated as counter-electrode in DSSCs. Indeed, Mali *et al.* have successfully synthesized PVP- and CA (cellulose acetate)-assisted  $\text{Cu}_2\text{ZnSnS}_4$  (CZTS) NFs via an electrospinning technique.

Surface morphology reveals that the PVP-assisted CZTS NFs have a smooth surface and that the diameters of the fibers can be

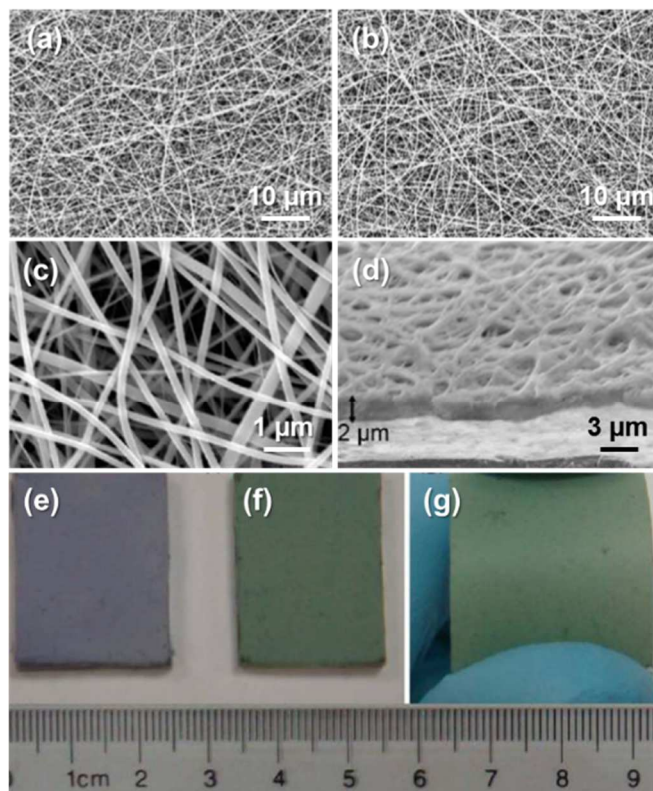


**Fig. 12** SEM images of the top views (a and b) of the PANI-PLA and PANI-CSA-PLA film on FTO glass, the magnified part (c) and crosssectional view (d) of the PANI-CSA-PLA nanofiber film, and the photos of the PANI-PLA/FTO (e), PANI-CSA-PLA/FTO (f), and PANI-CSA-PLA/PEN (g), respectively. Reproduced with permission from ref[152]. Copyright 2012 The Royal Society of Chemistry.

adjusted from 100-150 nm to 10-20 nm diameters just by swapping from PVP to CA matrix. The XRD and TEM results revealed that the PVP-assisted CZTS NFs are single kesterite crystalline, whereas CA-assisted CZTS NFs are kesterite polycrystalline in nature. Promising performances in solar cells close to 3.9% were obtained with these Pt-free electrodes.<sup>155</sup>

### 3.4 Electrospun materials for flexible DSSC

The integration of electronic devices into everyday objects that are non-planar and foldable can open new areas of application. Therefore flexible electronics have extensively investigated in the last decade for displays, thin-film transistor, batteries, solar cell, and others. The development of lightweight and mechanically resilient solar power sources is of increasing interest for transportable applications.<sup>156</sup> Typically in flexible devices the electrode is deposited on conducting plastic substrate. However, thermal degradation at high temperatures of most of the polymers used for the fabrication of the plastic substrates prevents the development of flexible DSSCs. Here the critical challenge is to achieve the good connectivity of  $\text{TiO}_2$  particles in a photo-electrode fabricated by a low-temperature process (below 150 °C) because most of the plastic substrates suffer from thermal degradation at the high temperatures (>450 °C) employed in the conventional sintering process. Several low-temperature methods such as chemical sintering<sup>157</sup> or mechanical pressing<sup>158</sup> have been proposed to improve the interconnectivity of  $\text{TiO}_2$  nanoparticles. Nevertheless, the degree of interconnectivity of particles or the adhesion between the resulting photoelectrode film and the substrate remain often



## ARTICLE

unsatisfactory. To tackle this challenge, in 2012, Li. *et al.* suggested a novel, low-temperature process for the fabrication of photo-electrodes composed of reinforced electrospun polyvinylidene fluoride (PVDF) fibers and TiO<sub>2</sub> NPs. Fig. 13(a) shows the spray-assisted electrospinning as a novel process of PVDF/TiO<sub>2</sub> NPs composite.<sup>159</sup> The as-spun PVDF NFs with diameters of ca. 400 nm were synthesized by electrospinning, as shown in Fig. 13(b). Surface analysis of the as-spun PVDF/TiO<sub>2</sub> NPs composite fibers (CFs), demonstrated that TiO<sub>2</sub> NPs were uniformly sprayed in pore volume between the NFs. This material was tested with respect to organic binder-free films (BFs) which are conventional electrodes for flexible DSSCs processed at low-temperature. The PCE of these solar cells was poor, around 1%, however the PVDF/TiO<sub>2</sub> photoanode revealed superior mechanical properties and a high stability even after 1000 bending cycles. Further developments on flexible substrates were achieved by implementing a bilayer photoanodic film composed of carbon nanotubes with TiO<sub>2</sub> nanorods as under layer and branched TiO<sub>2</sub> nanotubes as a light scattering top layer. Flexible DSSCs were fabricated using these materials by combining electrospray deposition, compression, and microwave treatment at low temperature (< 150°C) leading to PCE close to 4.2%.<sup>160</sup>

Apart from the low temperature of processing that are required by plastic substrates, the brittleness of inorganic photo-electrodes is another major problem that results in fractures and delamination under external bending forces. Consequently, under deformation the DSSCs show usually poor mechanical stability. To overcome this problem the development of nanowire morphology with an orientation perpendicular to the substrate seems preferable. Indeed this configuration allows to gain crack resistance, due to the efficient release of bending stress.<sup>161</sup> However the implementation of electrospinning techniques for the preparation of vertically oriented nanostructures remains challenging. Another interesting approach consists in developing polymer-TiO<sub>2</sub> hybrid composites<sup>162</sup> or TiO<sub>2</sub>-inorganic photoelectrodes showing higher mechanical robustness. This strategy appears indeed more compatible with electrospinning process. To illustrate this, one can mention the work of Zhu *et al.* who reported a photoanode that combines excellent bendability and flexibility and high-temperature durability.<sup>163</sup>

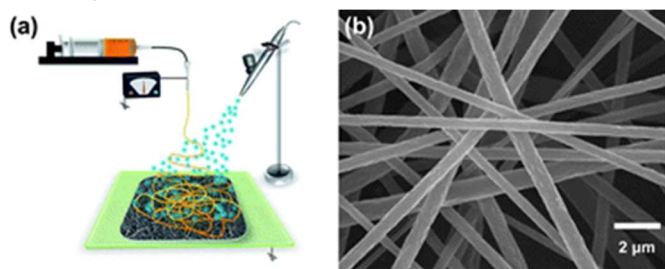


Fig. 13 (a) Spray-assisted electrospinning system. SEM images of (b) as-spun PVDF nanofibers. Reprinted with permission from ref [159]. Copyright 2012 The Royal Society

These authors reported a hybrid mat consisting of anatase-phased TiO<sub>2</sub> nanofibers and amorphous SiO<sub>2</sub> nanofibers prepared via the method of dual-spinneret electrospinning followed by pyrolysis. The hybrid fibrous mat was impregnated with binder-free TiO<sub>2</sub> nanoparticles and sintered at 480 °C to form a flexible composite photoanode for DSSC. The freestanding hybrid mat of TiO<sub>2</sub>-SiO<sub>2</sub> nanofibers was then pressed on ITO/PET and after sintering at 150 °C, a flexible and bendable photoanode film was obtained. The performances of the corresponding flexible devices were rather low, around 1%, but the free-standing mesoporous electrodes developed in this work allow to envision future developments of substrate-free flexible DSSC.

## 4. Other types of photovoltaic devices

### 4.1 Organic Solar Cells

Organic bulk-heterojunction (BHJ) solar cells are devices usually fabricated by mixing p-type organic semi-conductors (such as a pi-conjugated polymer or a small molecule) and n-type semiconductors (that can be a fullerene derivative, a small molecule or a polymer). In organic BHJ solar cell electrospinning techniques have been rarely explored compared to DSSC developments. However one can cite some works that were devoted to the preparation of electrodes, electron transport layer, and also the photoactive layer of the devices.

Since 2010, electrospinning was used as a tool to fabricate NFs made of either, coaxially assembled P3HT and PCBM,<sup>164,165</sup> or pure PCDTB.<sup>166</sup> P3HT-PCBM blends are not directly electrospinnable. To overcome this problem, in 2012, P3HT:PCBM-containing fibers were produced in a coaxial fashion by utilizing Poly(CaproLactone) (PCL) as an electrospinnable sheath material (Fig. 14).<sup>164</sup> The pure P3HT:PCBM fibers were obtained after electrospinning by selectively removing the PCL sheath with cyclopentanone. The resulting fibers show an average diameter  $120 \pm 30$  nm. They were incorporated into the active layer of a BHJ device, and this resulted in improved operating parameters and PCE, as compared to thin-film devices of identical chemical composition. The best-performing fiber-based devices exhibited a PCE of 4%. This increased performance was related to the in-plane alignment of P3HT polymer chains within the fibers resulting from the electrospinning process, which leads to increased optical absorption and subsequent exciton generation. The NFs of PCDTBT of different diameter were obtained following a similar strategy with a sacrificial poly(ethylene oxide) (PEO) matrix which is electrospun along the active polymer.

**Table 5.** Photovoltaic performances and electrochemical parameters of electrospun counter electrode based device

Counter electrode materials	J <sub>sc</sub> [mA.cm <sup>-2</sup> ]	V <sub>oc</sub> [V]	FF [%]	η [%]	R <sub>s</sub> [Ω.cm <sup>2</sup> ]	R <sub>CT</sub> [Ω.cm <sup>2</sup> ]	ref
CNFs/FTO	12.60	0.76	57	5.50	5.12	0.90	141
ref Pt/FTO	13.02	0.75	71	6.97	2.00	1.89	
CNFs	12.98	0.89	54	6.30	4.12	0.44	142
CNFs-Pt	14.53	0.83	67	8.00	3.16	0.175	
Ref. Pt	14.27	0.81	61	7.00	3.31	1.15	
Ni NP-CNT-CNFs/FTO	15.83	0.80	63	7.96	5.96	0.355	148
ref Pt/FTO	15.01	0.83	67	8.32	5.77	0.9	
TiC-C/FTO	12.30	0.66	37	2.95	3.92	68.6	143
Pt NP-TiC-CN/FTO	14.40	0.78	64	7.21	2.71	1.4	
Ref. Pt/FTO	14.80	0.77	66	7.54	2.29	0.7	
GCN 5 μm	14.52	0.77	64	7.15	3.63	0.49	144
GCN-Pt 5 μm	18.70	0.78	67	9.77	3.16	0.12	
Ref. Pt/FTO	17.20	0.79	63	8.63	3.27	1.3	
CN-(Fe-Ni)	10.1	0.72	65	4.6	7.50	3.01	149
CN	7.3	0.74	58	3.1	10.06	9.12	
Ref. Pt	9.8	0.71	66	4.6	5.07	3.12	
CN-(Cr-Co)/FTO	8.784	0.685	54	3.27	5.975	47.55	150
CN-(Ni-Co)/FTO	11.12	0.74	54	4.47	6.3	3.9	151
Ref Pt/FTO	16.12	0.718	51	5.90	-	-	
PANI-PLA/FTO	4.70	0.65	52	1.60	19.5	10.6	152
PANI-CSA-PLA/FTO	12.01	0.70	63	5.30	16.7	2.4	
Ref. Pt/FTO	13.88	0.70	67	6.51	15.5	2.1	
PANI-CSA-PLA/ITO (flexible substrate)	7.65	0.70	58	3.10	-	-	
Pt/ITO (flexible substrate)	10.38	0.70	61	4.39	-	-	
Pt NF (9 min) (FTO free)	12.30	0.81	54	5.30	18.7	30.2	153
Pt NF (12 min) (FTO free)	12.30	0.81	60	6.00	17.9	25.8	
ref Pt/FTO	12.50	0.80	66	7.20	15.8	9.65	
Pt (40 Ω.sq <sup>-1</sup> )	9.6	0.58	47	2.63	115 <sup>a</sup>	189.8 <sup>a</sup>	154
Pt (140 Ω.sq <sup>-1</sup> )	10.99	0.66	53	3.82	130.2 <sup>a</sup>	286.1 <sup>a</sup>	
Pt (250 Ω.sq <sup>-1</sup> )	10.95	0.66	48	3.47	176.4 <sup>a</sup>	482.3 <sup>a</sup>	
Pt/FTO	11.36	0.65	56	4.13	106.1 <sup>a</sup>	86.96 <sup>a</sup>	
PVP-CZTS/FTO	6.83	0.577	64	3.10	73	-	155
CA-CZTS/FTO	8.42	0.574	65	3.90	69	-	
Pt:FTO	4.66	0.623	57	1.72	96	-	

*a* in Ω.

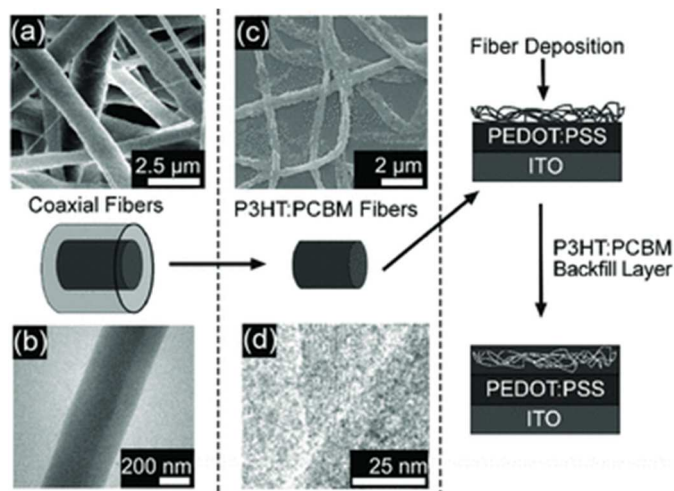


**Fig. 14** A schematic depicting P3HT:PCBM fiber generation from the coaxial fibers and the subsequent deposition of nanofibers within the active layer of the BHJ-OPV device, along with a) a scanning electron microscope (SEM) micrograph; b) a TEM micrograph of P3HT:PCBM (core)-PCL (sheath) fibers (2.5  $\mu\text{m}$  and 200 nm scale bars, respectively); c) an SEM micrograph of P3HT:PCBM nanofibers after removal of the PCL sheath (2  $\mu\text{m}$  scale bar), and; d) a high-resolution TEM micrograph of the P3HT:PCBM fibers after removal of the sheath PCL (25 nm scale bar). Reproduced with permission from ref [164]. Copyright 2012 Wiley.

PCDTBT:PEO NFs were electrospun onto a neat layer of PCDTB and after selective removal of PEO, PCBM was spin-coated onto the fibers to complete the active layer. The higher  $J_{\text{sc}}$  of 11.54  $\text{mA}\cdot\text{cm}^{-2}$  for the cell with NFs (compared to 9.95  $\text{mA}\cdot\text{cm}^{-2}$  for conventional BHJ solar cell), was attributed to better exciton dissociation and charge transport. This was observed for the NFs with the lower diameter of 20 nm which dimension is close to exciton diffusion length in organic materials. Some parameters such as the relative humidity level during the electrospinning process were investigated.<sup>167</sup> Indeed Kim *et al.* studied the impact of external conditions on the formation of P3HT:PEO NFs. They found that humidity rate modifies the kinetic of evaporation of the solvent during the process and therefore the structure of the final NFs. When humidity is high beads of pure P3HT are formed at the surface of NFs and as the consequence the photo-conversion efficiency of the corresponding devices drops significantly.

Apart from the materials of the active layer, electrode materials were also investigated. In particular some NWs were made of copper by electrospinning. In this work  $\text{CuAc}_2/\text{PVAc}$  was electrospun on the substrate.<sup>168</sup> After a calcination step in ambient conditions  $\text{CuO}$  NFs are obtained and subsequently annealed under  $\text{H}_2$  atmosphere to give rise to pure  $\text{Cu}$  NFs with diameter of 100 nm. The  $\text{Cu}$  NWs are well-interconnected and the transmittance as well as the sheet resistance of the resulting electrodes can be adjusted by playing with the NFs coverage of

the surface. This copper electrode compares favourably to other type of electrodes such as graphene-based electrodes which possess higher sheet resistance for similar transmittance. Moreover unlike ITO, the transmittance is relatively flat along the visible spectrum which is valuable for photovoltaic application. The potential of the  $\text{Cu}$ -electrode was evaluated in BHJ device configuration with P3HT/PCBM as an active layer leading to a promising PCE of 3%. Interestingly the  $\text{Cu}$ -NFs electrodes also exhibit good mechanical properties allowing their implementation on flexible substrate.  $\text{ZnO}$  was also investigated as an electron collecting electrode in BHJ devices because this semi-conductor possesses a high electron mobility. Elumalai *et al.* fabricated  $\text{ZnO}$  NWs electron transport layers in inverted organic solar cells.<sup>169</sup> The 1D structure of  $\text{ZnO}$  NWs greatly enhances charge collection compared to  $\text{ZnO}$  NPs. The NFs contributed to a better charge collection and FF leading to performances close to 3.5%.

#### 4.2 Electrospun materials for perovskite solar cells

Metalorganic lead halide perovskites have emerged recently as a very promising class of hybrid materials for photovoltaics. Indeed perovskite solar cells combine high efficiency (>18%) with low cost fabrication via low-temperature solution processes. Perovskites can be integrated in various device configurations including the ones inspired by DSSCs and BHJ solar cells. Similarly to DSSC most of the approaches that include electrospun materials in perovskite solar cells concern the fabrication of the mesoporous photoanode. Dharani *et al.* prepared and used electrospun  $\text{TiO}_2$  NFs mats as photoanode and studied the effect of the  $\text{TiO}_2$  film thickness after sensitization with perovskite. They demonstrated a PCE of 9.82% for thicknesses of *circa* 400 nm.<sup>170</sup>

Later, Mahmood *et al.* made a hyper-branched  $\text{TiO}_2$  photoanode by using a procedure that combined electrospinning and a hydrothermal method to grow NRs on the spun NFs.<sup>171</sup> An impressive PCE of 15.5% was obtained with a perovskite sensitizer using this unique hyper-branched structure. The technique was further extended by adding extra layers of these hyper-branched NFs to give thicker photoanode. The results with perovskite were disappointing because of the difficulty to grow perovskite in the pores, but using N719 as a sensitizer a PCE of 11.2% was demonstrated.

The hyper-branched structure exhibits higher diffusion coefficient and longer electron lifetime compared to simple NFs and conventional NPs. In order to overcome the poor pore filling with perovskite in the mesoporous photoanode, Xiao *et al.* developed a process to grow  $\text{CH}_3\text{NH}_3\text{PbI}_3$  perovskite directly onto  $\text{TiO}_2$  NFs.<sup>172</sup> First  $\text{TiO}_2:\text{PbO}$  doped NFs were prepared by electrospinning, then the mats were dipped into HI solution and

dried.  $\text{TiO}_2:\text{PbI}_2$  NFs were obtained and these fibers were subsequently used as a substrate to spin-coat a solution a  $\text{PbI}_2$  on top. After this step the material was then immersed in a solution of  $\text{CH}_3\text{NH}_3\text{I}$  to form the  $\text{CH}_3\text{NH}_3\text{PbI}_3$  perovskite layer. This method allowed the author to have a relatively high thickness of mesoporous film and therefore have better light harvesting. This strategy was successful and diminished the loss of photo-generated electrons thanks to the efficient collection and transport of charges in the NFs. Photo-conversion efficiency reached 9% without using any hole transporting material. Similarly to DSSCs some work has also been done on alternative metal oxide such as  $\text{Zn}_2\text{SnO}_4$ . Following previously described methods,  $\text{Zn}_2\text{SnO}_4$  NFs were prepared through electrospinning techniques. Highly porous fibers were obtained after calcination at 700 °C and then used for sensitization with perovskite. A maximum PCE of 7.38% was obtained for the best cell but interestingly it was shown a moderate hysteresis compared to NPs-based devices.<sup>173</sup>

So far no electrospun  $\text{CH}_3\text{NH}_3\text{PbI}_3$  perovskite material has been obtained however some perovskite made of bismuth ferrite were successfully synthesized by electrospinning by Fei *et al.*<sup>174</sup> Up to now these material has showed low photovoltaic effect.

## Conclusion and outlook

In this review, we summarize almost all aspects of electrospun materials for application in emerging solar cells technologies including dye-sensitized solar cells, organic solar cells and perovskite solar cells. The synthesis of novel materials, the development of fabrication procedures leading to unique nanostructures, the determination of their properties and performances in real devices and the latest developments are presented in details underlining the valuable contribution of electrospinning to the development of innovative and efficient materials for solar energy conversion. The increasing success of electrospinning as a tool for engineering nanomaterials is strongly related to the versatility of the technique that allows the preparation of a large variety of systems. The chemical composition, the shape, the crystallinity, the orientation and the surface coverage of electrospun materials can be easily controlled by adjusting key parameters. So far, most of the examples in the field of solar cells are dealing with the preparation of nanostructured electrode materials in DSSCs but electrospinning has been successfully employed more recently to fabricate organic bulk-heterojunction solar cells and perovskite solar cells. These developments open new doors for future laboratory research and improvement in solar energy conversion systems.

In other field of application such as energy storage devices, the market of electrospun materials is predicted to grow gradually and considerably owing to the advantages of the technique as discussed above. Besides, in the last decade, electrospinning machines compatible with industrial processes have been developed to realize large-scale production of electrospun fibers. Therefore it is expected that photovoltaic technologies will take benefit from these recent developments.

The increasing development of electrospun materials and methods in laboratory research and industry will surely contribute to push forthcoming electrospinning products with low cost and low environmental impact toward industrialization in the field of energy conversion systems.

## Acknowledgements

R.D. and I.D.K. acknowledge CEA and KIST for initiating this collaboration through the Nanosciences Research Program. Acknowledgment is made to the Campus France and Egide for partial financial support of this research through the STAR research program (Grant number 21443NJ). RD and IDK acknowledges Prof. N. Stingelin and S. Keltie for invitation to submit this feature article.

## References

- 1 B. Sun, Y.-Z. Long, Z.-J. Chen, S.-L. Liu, H.-D. Zhang, J.-C. Zhang and W.-P. Han, *J. Mater. Chem. C*, 2014, **2**, 1209–1219.
- 2 P. Jian, Y. Chiu, H. Sun, T. Chen, W. Chen and S. Tung, *ACS Appl. Mater. Interfaces*, 2014, **6**, 5506–5515.
- 3 Z. M. Huang, Y. Z. Zhang, M. Kotaki and S. Ramakrishna, *Compos. Sci. Technol.*, 2003, **63**, 2223–2253.
- 4 R. Sahay, P. S. Kumar, R. Sridhar, J. Sundaramurthy, J. Venugopal, S. G. Mhaisalkar and S. Ramakrishna, *J. Mater. Chem.*, 2012, **22**, 12953.
- 5 X. Lu, W. Zhang, C. Wang, T.-C. Wen and Y. Wei, *Prog. Polym. Sci.*, 2011, **36**, 671–712.
- 6 S. Dong, X. Chen, L. Gu, L. Zhang, X. Zhou, Z. Liu, P. Han, H. Xu, J. Yao, X. Zhang, L. Li, C. Shang and G. Cui, *Biosens. Bioelectron.*, 2011, **26**, 4088–4094.
- 7 P. J. Hall, M. Mirzaeian, S. I. Fletcher, F. B. Sillars, A. J. R. Rennie, G. O. Shitta-Bey, G. Wilson, A. Cruden and R. Carter, *Energy Environ. Sci.*, 2010, **3**, 1238–1251.
- 8 S. Cavaliere, S. Subianto, I. Savych, D. J. Jones and J. Rozière, *Energy Environ. Sci.*, 2011, **4**, 4761–4785.
- 9 W. T. Hong, M. Risch, K. A. Stoerzinger, A. Grimaud, || Jin Suntivich and Y. Shao-Horn, *Energy Environ. Sci.*, 2013, **8**, 1404–1427.
- 10 L. Cui, Y. Yang, C. Hsu and Y. Cui, *Nano Lett.*, 2009, **9**, 3370–3374.
- 11 D. Aradilla, M. Delaunay, S. Sadki, J.-M. Gérard and G. Bidan, *J. Mater. Chem. A*, 2015, **3**, 19254–19262.
- 12 D. P. Dubal, D. Aradilla, G. Bidan, P. Gentile, T. J. S. Schubert, J. Wimberg, S. Sadki and P. Gomez-Romero, *Sci. Rep.*, 2015, **5**, 9771.
- 13 Z. Ning, Y. Fu and H. Tian, *Energy Environ. Sci.*, 2010, **3**, 1170–1181.
- 14 M. Grätzel, *Acc. Chem. Res.*, 2009, **42**, 1788–1798.
- 15 Z. Dong, S. J. Kennedy and Y. Wu, *J. Power Sources*, 2011, **196**, 4886–4904.
- 16 F. Ma, Y. Ou, Y. Yang, Y. Liu, S. Xie, J.-F. Li, G. Cao, R. Proksch and J. Li, *J. Phys. Chem. C*, 2010, **114**, 22038–22043.

- 17 J.F. Cooley, 1900, Patent, GB 06385.
- 18 A. Formhals, A.1934, Patent, US 1975504.
- 19 J. Xie, K. M. R. Macewan, K. W. Z. Ray, W. Liu, D. Y. Siewe and Y. Xia, *ACS Nano*, 2010, **4**, 5027–5036.
- 20 J.-W. Jung, C.-L. Lee, S. Yu and I.-D. Kim, *J. Mater. Chem. A*, 2016, **4**, 703–750.
- 21 A. L. Yarin, S. Koombhongse and D. H. Reneker, *J. Appl. Phys.*, 2001, **90**, 4836–4846.
- 22 V. Aravindan, J. Sundaramurthy, P. Suresh Kumar, Y.-S. Lee, S. Ramakrishna and S. Madhavi, *Chem. Commun.*, 2015, **51**, 2225–2234.
- 23 D. Li and Y. Xia, *Nano Lett.*, 2003, **3**, 555–560.
- 24 N. Bhardwaj and S. C. Kundu, *Biotechnol. Adv.*, 2010, **28**, 325–347.
- 25 S. M. Jo, M. Y. Song, Y. R. Ahn, C. R. Park and D. Y. Kim, *J. Macromol. Sci. Part A Pure Appl. Chem.*, 2005, **42**, 1529–1540.
- 26 J. Shin, S. J. Choi, I. Lee, D. Y. Youn, C. O. Park, J. H. Lee, H. L. Tuller and I. D. Kim, *Adv. Funct. Mater.*, 2013, **23**, 2357–2367.
- 27 D. Li and Y. Xia, *Nano Lett.*, 2004, **4**, 933–938.
- 28 H. Chen, N. Wang, J. Di, Y. Zhao, Y. Song and L. Jiang, *Langmuir*, 2010, **26**, 11291–11296.
- 29 Y. Zhao, X. Cao and L. Jiang, *J. Am. Chem. Soc.*, 2007, **129**, 764–5.
- 30 I. D. Kim, A. Rothschild, B. H. Lee, D. Y. Kim, S. M. Jo and H. L. Tuller, *Nano Lett.*, 2006, **6**, 2009–2013.
- 31 B. O'Regan and M. Grätzel, *Nature*, 1991, **353**, 737–740.
- 32 H. Tsubomura, M. Matsumura, Y. Nomura and T. Amamiya, *Nature*, 1976, **261**, 402–403.
- 33 B. E. Hardin, J. Snaith and M. D. McGehee, *Nat. Photonics*, 2012, **6**, 162–169.
- 34 D. Joly, L. Pelleja, S. Narbey, F. Oswald, T. Meyer, Y. Kervella, P. Maldivi, J. N. Clifford, E. Palomares and R. Demadrille, *Energy Environ. Sci.*, 2015, **8**, 2010–2018.
- 35 A. Fakharuddin, R. Jose, T. M. Brown, F. Fabregat-Santiago and J. Bisquert, *Energy Environ. Sci.*, 2014, **7**, 3952–3981.
- 36 S. Ardo and G. J. Meyer, *Chem. Soc. Rev.*, 2009, **38**, 115–164.
- 37 A. Hagfeldt, G. Boschloo, L. Sun, L. Kloo and H. Pettersson, *Chem. Rev.*, 2010, **110**, 6595–6663.
- 38 J.-H. Yum, E. Baranoff, S. Wenger, M. K. Nazeeruddin and M. Grätzel, *Energy Environ. Sci.*, 2011, **4**, 842–857.
- 39 K. Onozuka, B. Ding, Y. Tsuge, T. Naka, M. Yamazaki, S. Sugi, S. Ohno, M. Yoshikawa and S. Shiratori, *Nanotechnology*, 2006, **17**, 1026–1031.
- 40 C. Richter and C. A. Schmittenmaer, *Nat. Nanotechnol.*, 2010, **5**, 769–772.
- 41 M. Y. Song, Y. R. Ahn, S. M. Jo, D. Y. Kim and J. P. Ahn, *Appl. Phys. Lett.*, 2005, **87**, 113113.
- 42 M. Y. Song, D. K. Kim, K. J. Ihn, S. M. Jo and D. Y. Kim, *Nanotechnology*, 2004, **15**, 1861–1865.
- 43 P. Du, L. Song, J. Xiong and C. Cui, *Surf. Interface Anal.*, 2013, **45**, 1878–1883.
- 44 D. Hwang, S. M. Jo, D. Y. Kim, V. Armel, D. R. MacFarlane and S. Jang, *ACS Appl. Mater. Interfaces*, 2011, **3**, 1521–1527.
- 45 B. H. Lee, M. Y. Song, S. Jang, S. M. Jo, S. Kwak and D. Y. Kim, *J. Phys. Chem. C*, 2009, **113**, 21453–21457.
- 46 S. H. Hwang, C. Kim, H. Song, S. Son and J. Jang, *ACS Appl. Mater. Interfaces*, 2012, **4**, 5287–5292.
- 47 A. S. Nair, P. Zhu, V. Jagadeesh Babu, S. Yang, T. Krishnamoorthy, R. Murugan, S. Peng and S. Ramakrishna, *Langmuir*, 2012, **28**, 6202–6206.
- 48 Y. P. Lin, Y. Y. Chen, Y. C. Lee and Y. W. Chen-Yang, *J. Phys. Chem. C*, 2012, **116**, 13003–13012.
- 49 H. Chen, T. Zhang, J. Fan, D. Kuang and C. Su, *ACS Appl. Mater. Interfaces*, 2013, **5**, 9205–9211.
- 50 a S. Nair, S. Yang, P. Zhu and S. Ramakrishna, *Chem. Commun. (Camb.)*, 2010, **46**, 7421–7423.
- 51 Y. Shengyuan, Z. Peining, a. S. Nair and S. Ramakrishna, *J. Mater. Chem.*, 2011, **21**, 6541–6548.
- 52 G. S. Anjusree, A. Bhupathi, A. Balakrishnan, S. Vadukumpully, K. R. V Subramanian, N. Sivakumar, S. Ramakrishna, S. V Nair and A. S. Nair, *Rsc Adv.*, 2013, **3**, 16720–16727.
- 53 H. Krysova, J. Trckova-Barakova, J. Prochazka, A. Zukal, J. Maixner and L. Kavan, *Catal. Today*, 2014, **230**, 234–239.
- 54 B. R. Koo, H. An and H. J. Ahn, *Ceram. Int.*, 2016, **42**, 1666–1671.
- 55 X. Zhang, V. Thavasi, S. G. Mhaisalkar and S. Ramakrishna, *Nanoscale*, 2012, **4**, 1707–1716.
- 56 X. Wang, G. He, H. Fong and Z. Zhu, *J. Phys. Chem. C*, 2013, **117**, 1641–1646.
- 57 W. Zhang, R. Zhu, L. Ke, X. Liu, B. Liu and S. Ramakrishna, *Small*, 2010, **6**, 2176–2182.
- 58 P. S. Kumar, S. A. S. Nizar, J. Sundaramurthy, P. Ragupathy, V. Thavasi, S. G. Mhaisalkar and S. Ramakrishna, *J. Mater. Chem.*, 2011, **21**, 9784–9790.
- 59 Y. P. Lin, S. Y. Lin, Y. C. Lee and Y. W. Chen-Yang, *J. Mater. Chem. A*, 2013, **1**, 9875–9884.
- 60 S. S. Mali, C. S. Shim, H. Kim, J. V. Patil, D. H. Ahn, P. S. Patil and C. K. Hong, *Electrochem. Acta*, 2015, **166**, 356–366.
- 61 S. Chuangchote, T. Sagawa and S. Yoshikawa, *Appl. Phys. Lett.*, 2008, **93**, 033310.
- 62 J.-H. Lee, K. Ahn, S. H. Kim, J. M. Kim, S.-Y. Jeong, J.-S. Jin, E. D. Jeong and C.-R. Cho, *Curr. Appl. Phys.*, 2014, **14**, 856–861.
- 63 G. Zhu, L. Pan, J. Yang, X. Liu, H. Sun and Z. Sun, *J. Mater. Chem.*, 2012, **1**, 24326–24329.
- 64 P. Joshi, L. Zhang, D. Davoux, Z. Zhu, D. Galipeau, H. Fong and Q. Qiao, *Energy Environ. Sci.*, 2010, **3**, 1507–1510.
- 65 H. Gao, C. X. Bao, T. Yu, Y. F. Yao, F. M. Li, Y. J. Yuan, J. G. Liu and Z. G. Zou, *Rsc Adv.*, 2014, **4**, 10519–10524.
- 66 X. Liu, J. Fang, M. Gao, H. Wang, W. Yang and T. Lin, *Mater. Chem. Phys.*, 2015, **151**, 330–336.
- 67 G. Wang, W. Xiao and J. Yu, *Energy*, 2015, **86**, 196–203.
- 68 L. Yang and W. W. F. Leung, *Adv. Mater.*, 2011, **23**, 4559–4562.
- 69 P. Zhu, a. S. Nair, S. Yang, S. Peng and S. Ramakrishna, *J. Mater. Chem.*, 2011, **21**, 12210–12212.
- 70 A. S. Nair, R. Jose, Y. Shengyuan and S. Ramakrishna, *J. Colloid Interface Sci.*, 2011, **353**, 39–45.

- 71 T. Krishnamoorthy, V. Thavasi, M. Subodh G and S. Ramakrishna, *Energy Environ. Sci.*, 2011, **4**, 2807–2812.
- 72 J. S. Tobin, a. J. Turinske, N. Stojilovic, a. F. Lotus and G. Chase, *Curr. Appl. Phys.*, 2012, **12**, 919–923.
- 73 R. a. Naphade, M. Tathavadekar, J. P. Jog, S. Agarkar and S. Ogale, *J. Mater. Chem. A*, 2014, **2**, 975–984.
- 74 S. H. Nam, H. S. Shim, Y. S. Kim, M. A. Dar, J. G. Kim and W. B. Kim, *ACS Appl. Mater. Interfaces*, 2010, **2**, 2046–2052.
- 75 S. Cavaliere, S. Subianto, L. Chevallier, D. J. Jones and J. Rozière, *Chem. Commun. (Camb)*, 2011, **47**, 6834–6836.
- 76 P. S. Archana, R. Jose, T. M. Jin, C. Vijila, M. M. Yusoff and S. Ramakrishna, *J. Am. Ceram. Soc.*, 2010, **93**, 4096–4102.
- 77 P. S. Archana, E. Naveen Kumar, C. Vijila, S. Ramakrishna, M. M. Yusoff and R. Jose, *Dalton Trans.*, 2013, **42**, 1024–1032.
- 78 P. S. Archana, A. Gupta, M. M. Yusoff and R. Jose, *Phys. Chem. Chem. Phys.*, 2014, **16**, 7448–7454.
- 79 B. Ding and J. Yu, *Electrospun Nanofibers for Energy and Environmental Applications*, Heidelberg New York Dordrecht London, 2014.
- 80 J. Li, X. Chen, N. Ai, J. Hao, Q. Chen, S. Strauf and Y. Shi, *Chem. Phys. Lett.*, 2011, **514**, 141–145.
- 81 S. H. Hwang, H. Song, J. Lee and J. Jang, *Chem. - A Eur. J.*, 2014, **20**, 12974–12981.
- 82 A. A. Madhavan, S. Kalluri, D. K. Chacko, A. T. A, S. N, K. R. V. Subramanian, S. Nair, S. V Nair and A. Balakrishnan, *RSC Adv.*, 2012, **2**, 13032–13037.
- 83 M. Motlak, N. A. M. Barakat, M. S. Akhtar, A. M. Hamza, A. Yousef, H. Fouad and O. B. Yang, *Ceram. Int.*, 2015, **41**, 1205–1212.
- 84 M. Motlak, N. a. M. Barakat, M. S. Akhtar, A. G. El-Deen, M. Obaid, C. S. Kim, K. A. Khalil and A. a. Almajid, *Chem. Eng. J.*, 2015, **268**, 153–161.
- 85 P. Du, L. Song, J. Xiong, N. Li, L. Wang, Z. Xi, N. Wang, L. Gao and H. Zhu, *Electrochim. Acta*, 2013, **87**, 651–656.
- 86 L. Yang and W. W. F. Leung, *Adv. Mater.*, 2013, **25**, 1792–1795.
- 87 R. Jose, V. Thavasi and S. Ramakrishna, *J. Am. Ceram. Soc.*, 2009, **92**, 289–301.
- 88 A. Kay and M. Grätzel, *Chem. Mater.*, 2002, **14**, 2930–2935.
- 89 Y. P. Y. P. Ariyasinghe, T. R. C. K. Wijayarathna, I. G. C. K. Kumara, I. P. L. Jayarathna, C. A. Thotawatthage, W. S. S. Gunathilake, G. K. R. Senadeera and V. P. S. Perera, *J. Photochem. Photobiol. A Chem.*, 2011, **217**, 249–252.
- 90 P. Guo and M. a. Aegerter, *Thin Solid Films*, 1999, **351**, 290–294.
- 91 K. Sayama, H. Sugihara and H. Arakawa, *J. Phys. Chem. B*, 1998, **10**, 3825–3832.
- 92 K. Hara, T. Horiguchi, T. Kinoshita and K. Sayama, *Sol. Energy Mater. Sol. Cells*, 2000, **64**, 115–134.
- 93 K. Kakiuchi, E. Hosono and S. Fujihara, *J. Photochem. Photobiol. A Chem.*, 2006, **179**, 81–86.
- 94 Y. W. Heo, D. P. Norton, L. C. Tien, Y. Kwon, B. S. Kang, F. Ren, S. J. Pearton and J. R. Laroche, *Mater. Sci. Eng. R Reports*, 2004, **47**, 1–47.
- 95 C. F. Klingshirn, *ChemPhysChem*, 2007, **8**, 782–803.
- 96 L. Schmidt-Mende and J. L. MacManus-Driscoll, *Mater. Today*, 2007, **10**, 40–48.
- 97 K. Keis, E. Magnusson, H. Lindström, S. E. Lindquist and A. Hagfeldt, *Sol. Energy Mater. Sol. Cells*, 2002, **73**, 51–58.
- 98 N. Memarian, I. Concina, A. Braga, S. M. Rozati, A. Vomiero and G. Sberveglieri, *Angew. Chemie - Int. Ed.*, 2011, **50**, 12321–12325.
- 99 Q. F. Zhang, C. S. Dandeneau, X. Y. Zhou and G. Z. Cao, *Adv. Mater.*, 2009, **21**, 4087–4108.
- 100 J. Bouclé and J. Ackermann, *Polym. Int.*, 2012, **61**, 355–373.
- 101 I. D. Kim, J. M. Hong, B. H. Lee, D. Y. Kim, E. K. Jeon, D. K. Choi and D. J. Yang, *Appl. Phys. Lett.*, 2007, **91**, 163109.
- 102 W. Zhang, R. Zhu, X. Liu, B. Liu and S. Ramakrishna, *Appl. Phys. Lett.*, 2009, **95**, 043304.
- 103 M. McCune, W. Zhang and Y. Deng, *Nano Lett.*, 2012, **12**, 3656–3662.
- 104 L. Song, P. Du, J. Xiong, F. Ko and C. Cui, *Electrochim. Acta*, 2015, **163**, 330–337.
- 105 A. A. Madhavan, A. Mohandas, A. Licciulli, K. P. Sanosh, P. Praveen, R. Jayakumar, S. V Nair, A. S. Nair and A. Balakrishnan, *Rsc Adv.*, 2013, **3**, 25312–25316.
- 106 P. Du, L. Song, J. Xiong, N. Li, Z. Xi, L. Wang, D. Jin, S. Guo and Y. Yuan, *Electrochim. Acta*, 2012, **78**, 392–397.
- 107 T. Krishnamoorthy, M. Z. Tang, A. Verma, a. S. Nair, D. Pliszka, S. G. Mhaisalkar and S. Ramakrishna, *J. Mater. Chem.*, 2012, **22**, 2166–2172.
- 108 Y. Fukai, Y. Kondo, S. Mori and E. Suzuki, *Electrochem. commun.*, 2007, **9**, 1439–1443.
- 109 E. N. Kumar, R. Jose, P. S. Archana, C. Vijila, M. M. Yusoff and S. Ramakrishna, *Energy Environ. Sci.*, 2012, **5**, 5401–5407.
- 110 C. Gao, X. Li, B. Lu, L. Chen, Y. Wang, F. Teng, J. Wang, Z. Zhang, X. Pan and E. Xie, *Nanoscale*, 2012, **4**, 3475–3481.
- 111 X. Xia, X. J. Dong, Q. F. Wei, Y. B. Cai and K. Y. Lu, *Express Polym. Lett.*, 2012, **6**, 169–176.
- 112 S. Cavaliere, S. Subianto, I. Savych, M. Tillard, D. J. Jones and J. Rozière, *J. Phys. Chem. C*, 2013, **117**, 18298–18307.
- 113 C. Gao, X. Li, X. Zhu, L. Chen, Z. Zhang, Y. Wang, Z. Zhang, H. Duan and E. Xie, *J. Power Sources*, 2014, **264**, 15–21.
- 114 S. H. Ahn, D. J. Kim, W. S. Chi and J. H. Kim, *Adv. Mater.*, 2013, **25**, 4893–4897.
- 115 J. J. Wu, Y. R. Chen, W. P. Liao, C. Te Wu and C. Y. Chen, *ACS Nano*, 2010, **4**, 5679–5684.
- 116 R. Sharma, R. S. Mane, S. K. Min and S. H. Han, *J. Alloys Compd.*, 2009, **479**, 840–843.
- 117 A. Furube, M. Murai, S. Watanabe, K. Hara, R. Katoh and M. Tachiya, *J. Photochem. Photobiol. A Chem.*, 2006, **182**, 273–279.
- 118 C. Miao, C. Chen, Q. Dai, L. Xu and H. Song, *J. Colloid Interface Sci.*, 2015, **440**, 162–167.
- 119 S. Burnside, J.-E. J. E. Moser, K. Brooks, M. Grätzel and D. Cahen, *J. Phys. Chem. B*, 1999, **103**, 9328–9332.
- 120 F. Lenzmann, J. Krueger, S. Burnside, K. Brooks, M. Grätzel, D. Gal, S. Rühle and D. Cahen, *J. Phys. Chem. B*, 2001, **105**, 6347–6352.

- 121 D. Hou, X. Hu, W. Ho, P. Hu and Y. Huang, *J. Mater. Chem. A*, 2015, **3**, 3935–3943.
- 122 B. Tan, E. Toman, Y. Li and Y. Wu, *J. Am. Chem. Soc.*, 2007, **129**, 4162–4163.
- 123 Z. D. Li, Y. Zhou, C. X. Bao, G. G. Xue, J. Y. Zhang, J. G. Liu, T. Yu and Z. G. Zou, *Nanoscale*, 2012, **4**, 3490–3494.
- 124 L. Huang, L. Jiang and M. Wei, *Electrochem. commun.*, 2010, **12**, 319–322.
- 125 D. W. Kim, S. S. Shin, I. S. Cho, S. Lee, D. H. Kim, C. W. Lee, H. S. Jung and K. S. Hong, *Nanoscale*, 2012, **4**, 557–562.
- 126 S. H. Choi, D. Hwang, D. Y. Kim, Y. Kervella, P. Maldivi, S. Y. Jang, R. Demadrille and I. D. Kim, *Adv. Funct. Mater.*, 2013, **23**, 3146–3155.
- 127 D. Hwang, J.-S. Jin, H. Lee, H.-J. Kim, H. Chung, D. Y. Kim, S.-Y. Jang and D. Kim, *Sci. Rep.*, 2014, **4**, 7353.
- 128 O. A. Ileperuma, M. A. K. L. Dissanayake, S. Somasunderam and L. R. A. K. Bandara, *Sol. Energy Mater. Sol. Cells*, 2004, **84**, 117–124.
- 129 J. Y. Kim, T. H. Kim, D. Y. Kim, N. G. Park and K. D. Ahn, *J. Power Sources*, 2008, **175**, 692–697.
- 130 M. Biancardo, K. West and F. C. Krebs, *J. Photochem. Photobiol. A Chem.*, 2007, **187**, 395–401.
- 131 P. Wang, S. M. Zakeeruddin, I. Exnar and M. Grätzel, *Chem. Commun.*, 2002, **8**, 2972–2973.
- 132 A. R. S. Priya, A. Subramania, Y. Jung and K. Kim, *Langmuir*, 2008, **24**, 9816–9819.
- 133 S. K. Ahn, T. Ban, P. Sakthivel, J. W. Lee, Y.-S. Gal, M.-R. Kim, J.-K. Lee and S.-H. Jin, *ACS Appl Mater Interfaces*, 2012, **4**, 2096–2100.
- 134 E. Vijayakumar, A. Subramania, Z. Fei and P. J. Dyson, *RSC Adv.*, 2015, **5**, 52026–52032.
- 135 E. Vijayakumar, A. Subramania, Z. Fei and P. J. Dyson, *J. Appl. Polym. Sci.*, 2015, **132**, 42032.
- 136 V. Elayappan, V. Murugadoss, S. Angaiah, Z. Fei and P. J. Dyson, *J. Appl. Polym. Sci.*, 2015, **132**, 42777.
- 137 M. Sethupathy, P. Pandey and P. Manisankar, *J. Appl. Polym. Sci.*, 2014, **131**, 41107.
- 138 N. Papageorgiou, *J. Electrochem. Soc.*, 1997, **144**, 876–884.
- 139 D.-J. Yun, J. Kim, J. Chung, S. Park, W. Baek, Y. Kim, S. Kim, Y.-N. Kwon, J. Chung, Y. Kyoung, K.-H. Kim and S. Heo, *J. Power Sources*, 2014, **268**, 25–36.
- 140 E. Olsen, G. Hagen and S. Eric Lindquist, *Sol. Energy Mater. Sol. Cells*, 2000, **63**, 267–273.
- 141 P. Joshi, L. Zhang, Q. Chen, D. Galipeau, H. Fong and Q. Qiao, *ACS Appl. Mater. Interfaces*, 2010, **2**, 3572–3577.
- 142 P. Poudel, L. Zhang, P. Joshi, S. Venkatesan, H. Fong and Q. Qiao, *Nanoscale*, 2012, **4**, 4726–4730.
- 143 Y. Zhao, A. Thapa, Q. Feng, M. Xi, Q. Qiao and H. Fong, *Nanoscale*, 2013, **5**, 11742–11747.
- 144 H. Elbohy, A. Aboagye, S. Sigdel, Q. Wang, M. H. Sayyad, L. Zhang and Q. Qiao, *J. Mater. Chem. A*, 2015, **3**, 17721–17727.
- 145 Q. W. Jiang, G. R. Li, S. Liu and X. P. Gao, *J. Phys. Chem. C*, 2010, **114**, 13397–13401.
- 146 Y. Y. Dou, G. R. Li, J. Song and X. P. Gao, *Phys. Chem. Chem. Phys.*, 2012, **14**, 1339–1342.
- 147 R. Bajpai, S. Roy, N. Kulshrestha, J. Rafiee, N. Koratkar and D. S. Misra, *Nanoscale*, 2012, **4**, 926–930.
- 148 P. Joshi, Z. Zhou, P. Poudel, A. Thapa, X.-F. Wu and Q. Qiao, *Nanoscale*, 2012, **4**, 5659–5664.
- 149 K. Saranya, A. Subramania and N. Sivasankar, *RSC Adv.*, 2015, **5**, 43611–43619.
- 150 I. M. A. Mohamed, M. Motlak, M. S. Akhtar, A. S. Yasin, M. H. El-Newehy, S. S. Al-Deyab and N. A. M. Barakat, *Ceram. Int.*, 2016, **42**, 146–153.
- 151 M. Motlak, N. A. M. Barakat, M. S. Akhtar, A. M. Hamza, B.-S. Kim, C. S. Kim, K. A. Khalil and A. A. Almajid, *Electrochem. Acta*, 2015, **160**, 1–6.
- 152 S. Peng, P. Zhu, Y. Wu, S. G. Mhaisalkar and S. Ramakrishna, *RSC Adv.*, 2012, **2**, 652–657.
- 153 J. Kim, J. Kang, U. Jeong, H. Kim and H. Lee, *ACS Appl. Mater. Interfaces*, 2013, **5**, 3176–3181.
- 154 R. Zhou, W. Guo, R. Yu and C. Pan, *J. Mater. Chem. A*, 2015, **3**, 23028–23034.
- 155 S. S. Mali, P. S. Patil and C. K. Hong, *ACS Appl. Mater. Interfaces*, 2014, **6**, 1688–1696.
- 156 M. Kaltenbrunner, M. S. White, E. D. Głowacki, T. Sekitani, T. Someya, N. S. Sariciftci and S. Bauer, *Nat. Commun.*, 2012, **3**, 770.
- 157 H. C. Weerasinghe, P. M. Sirimanne, G. V. Franks, G. P. Simon and Y. B. Cheng, *J. Photochem. Photobiol. A Chem.*, 2010, **213**, 30–36.
- 158 T. Yamaguchi, N. Tobe, D. Matsumoto and H. Arakawa, *Chem. Commun. (Camb.)*, 2007, 4767–9.
- 159 Y. Li, D. K. Lee, J. Y. Kim, B. Kim, N. G. Park, K. Kim, J. H. Shin, I. S. Choi and M. J. Ko, *Energy Environ. Sci.*, 2012, **5**, 8950–8957.
- 160 L. Song, Y. Guan, P. Du, Y. Yang, F. Ko and J. Xiong, *Sol. Energy Mater. Sol. Cells*, 2016, **147**, 134–143.
- 161 C. Y. Jiang, X. W. Sun, K. W. Tan, G. Q. Lo, A. K. K. Kyaw and D. L. Kwong, *Appl. Phys. Lett.*, 2008, **92**, 143101.
- 162 Y. Li, K. Yoo, D. K. Lee, J. H. Kim, N. G. Park, K. Kim and M. J. Ko, *Curr. Appl. Phys.*, 2010, **10**, e171–e175.
- 163 X. Wang, M. Xi, H. Fong and Z. Zhu, *ACS Appl. Mater. Interfaces*, 2014, **6**, 15925–15932.
- 164 N. M. Bedford, M. B. Dickerson, L. F. Drummy, H. Koerner, K. M. Singh, M. C. Vasudev, M. F. Durstock, R. R. Naik and A. J. Steckl, *Adv. Energy Mater.*, 2012, **2**, 1136–1144.
- 165 C. Dillard, R. Singhal and V. Kalra, *Macromol. Mater. Eng.*, 2015, **300**, 320–327.
- 166 T. Kim, S. J. Yang, S. K. Kim, H. S. Choi and C. R. Park, *Nanoscale*, 2014, **6**, 2847–2854.
- 167 T. Kim, S. J. Yang, S. J. Sung, Y. S. Kim, M. S. Chang, H. Jung and C. R. Park, *ACS Appl. Mater. Interfaces*, 2015, **7**, 4481–4487.
- 168 H. Wu, L. Hu, M. W. Rowell, D. Kong, J. J. Cha, J. R. McDonough, J. Zhu, Y. Yang, M. D. McGehee and Y. Cui, *Nano Lett.*, 2010, **10**, 4242–4248.
- 169 N. K. Elumalai, T. M. Jin, V. Chellappan, R. Jose, S. K. Palaniswamy, S. Jayaraman, H. K. Raut and S. Ramakrishna, *ACS Appl. Mater. Interfaces*, 2013, **5**, 9396–404.

- 170 S. Dharani, H. K. Mulmudi, N. Yantara, P. T. Thu Trang, N. G. Park, M. Graetzel, S. Mhaisalkar, N. Mathews and P. P. Boix, *Nanoscale*, 2014, **6**, 1675–1679.
- 171 K. Mahmood, B. S. Swain and A. Amassian, *Adv. Mater.*, 2015, **27**, 2859–2865.
- 172 Y. Xiao, G. Han, Y. Li, M. Li and J. Wu, *J. Mater. Chem. A*, 2014, **2**, 16856–16862.
- 173 S. S. Mali, C. Su Shim and C. Kook Hong, *Sci. Rep.*, 2015, **5**, 11424.
- 174 L. Fei, Y. Hu, X. Li, R. Song, L. Sun, H. Huang, H. Gu, H. L. W. Chan and Y. Wang, *ACS Appl. Mater. Interfaces*, 2015, **7**, 3665–3670.

This feature article discusses highly promising and versatile electrospinning methods and electrospun materials employed for the fabrication of solar cells.

